

Validating Subglacial Volcanic Eruption Using Ground-Based C-Band Radar Imagery

Frank Silvio Marzano, *Senior Member, IEEE*, Mirko Lamantea, Mario Montopoli, Björn Oddsson, and Magnús Tumi Gudmundsson

Abstract—The main phase of the moderately sized November 2004 eruption of the Grímsvötn volcano, located in the center of the 8100 km² Vatnajökull glacier, was monitored by the Icelandic Meteorological Office C-band weather radar in Keflavík, 260 km west of the volcano. The eruption plume reached a height of 6–10 km relative to the vent. The distribution of the most distal tephra was measured in the autumn of 2004, while the deposition on the glacier was mapped in the summers of 2005 and 2006. The tephra formed a well-defined layer on the glacier in the region north and northeast of the craters. The total mass of the tephra layer is quantitatively compared with the retrieved values, obtained from an improved version of the volcanic ash radar retrieval (VARR) algorithm. VARR was statistically calibrated with ground-based ash size distribution samples, taken at Vatnajökull, and by taking into account both antenna beam occlusion and wind-driven plume advection. The latter was implemented by using a space–time image phase-based cross-correlation technique. Accuracy of the weather radar records was also reviewed, noting that a large variability in the plume height estimation may be obtained using different approaches. The comparisons suggest that, at least for this subglacial eruption, the surface tephra mass, estimated by using the VARR inversion approach, is in a fairly good agreement with *in situ* measurements in terms of spatial extension, distribution, and amount.

Index Terms—Ash retrieval, inversion methods, radar meteorology, volcanic eruption clouds, weather radars.

I. INTRODUCTION

THE detection and quantitative retrieval of volcanic ash clouds are of significant interest due to their impact

Manuscript received February 18, 2011; revised June 11, 2011 and August 10, 2011; accepted August 20, 2011. Date of publication October 6, 2011; date of current version March 28, 2012. This work was supported in part by the Italian Department of Civil Protection (DPC), Rome, Italy, within the IDRA project and in part by the Sapienza University of Rome, Rome.

F. S. Marzano is with the Department of Information Engineering, Electronics and Telecommunications, Sapienza University of Rome, 00184 Rome, Italy, and also with the Centro di Eccellenza per l'Integrazione di Tecniche di Telerilevamento e Modellistica Numerica per la Previsione di Eventi Meteorologici Severi (CETEMPS), University of L'Aquila, 67100 L'Aquila, Italy (e-mail: marzano@die.uniroma1.it).

M. Lamantea is with the Department of Information Engineering, Electronics and Telecommunications, Sapienza University of Rome, 00184 Rome, Italy (e-mail: mirkolamantea@gmail.com).

M. Montopoli is with the Department of Electrical and Information Engineering, 67100 L'Aquila, Italy and the Centro di Eccellenza per l'Integrazione di Tecniche di Telerilevamento e Modellistica Numerica per la Previsione di Eventi Meteorologici Severi (CETEMPS), University of L'Aquila, 67100 L'Aquila, Italy (e-mail: mario.montopoli@univaq.it).

B. Oddsson and M. T. Gudmundsson are with the Institute of Earth Sciences, University of Iceland, 101 Reykjavik, Iceland (e-mail: mtg@hi.is; bjornod@hi.is).

Color versions of one or more of the figures in this paper are available online at <http://ieeexplore.ieee.org>.

Digital Object Identifier 10.1109/TGRS.2011.2167017

on environment and human activities [1]. Volcanic eruptions also represent a serious socioeconomic threat because of the widespread disruption caused by the most violent explosive eruption clouds. Atmospheric contamination by volcanic ash may affect aircraft safety and has significant effects on air traffic control, making rerouting of airways necessary in proximity of the volcanic cloud [2]. Volcanic eruptions may have both short-term effects, regarding threats to people who live near the volcano, and long-term effects, because ash may drift for days or weeks in the atmosphere before fallout is completed, thus causing serious economic costs at local and medium distances (for example, to remove ash from buildings or farmlands) [3], [4].

Quantitative measurements and analyses of the physical and chemical properties of volcanic ash clouds are crucial. In this context, radar remote sensing through ground-based weather radar may represent a very powerful, and to some extent, unique instrument to study these phenomena in proximity of volcanic vents [5]–[7]. Coarse ash and lapilli are expected to fall within a few hours of ejection into the air and within distances less than a few hundred kilometers from the volcanic vent [9] and are often estimated to constitute more than 99% of the total ash mass [10]. The latter may be missed by retrieval algorithms based on satellite thermal-infrared split-window techniques which are insensitive to ash particles larger than 5 μm [3].

Weather radar targets are usually precipitating hydrometeors whose absorption and scattering effects on the radar transmitted microwave are measured by the radar itself [11]. Hydrometeor shape, dimension, and dielectric properties are undoubtedly different from tephra particles so that weather radar cannot be used for a reliable ash cloud monitoring without developing *ad hoc* algorithms, inversion methodologies, and techniques to process the radar data stream [12]. Among these algorithms, the volcanic ash radar retrieval (VARR) approach has been shown to be a general theoretical and operational framework with the aim to infer, in a quantitative way, ash mass category, concentration, and fallout rate from 3-D scanning weather-radar measurements [7].

This paper presents new results of the VARR algorithm, applied to the subglacial eruption of Icelandic Grímsvötn volcano that occurred in November 2004 and was measured by the Keflavík C-band weather radar at a distance of about 260 km from the volcano vent [13]–[15]. The main objective of this paper is to assess, for the first time to the authors' knowledge, a quantitative consistency between radar-based ash mass retrievals and ground measurements. The latter have been derived from the results of the Vatnajökull fieldwork carried out during the summers of 2005 and 2006 [16]. Measurements of the



Fig. 1. Tephra layer on Vatnajökull indicated over a georeferenced visible image, taken from MODIS aboard the satellite AQUA on November 7, 2004. The tephra deposit is covered with snow on Bárðabunga and northeast of Grímsvötn. The tephra is exposed on Dyngjujökull stretching to the northeast (MODIS image courtesy by J. Desloîtres, MODIS Rapid Response Team, NASA-Goddard Space Flight Center; <http://visibleearth.nasa.gov>).

tephra deposited on the Vatnajökull glacier, conserved within the 2004–2005 winter snow accumulation, were systematically performed by Icelandic teams and used in this work for ground validation of VARR radar retrievals [7], [13]. The VARR algorithm is improved by taking into account the ground sampling of ash particle size distributions (PSDs), the effect of wind transportation on the observed ash plume, and the occlusion of the antenna beamwidth due to mountain obstacles.

This paper is structured as follows. In Section II, the data obtained by ground sampling and probing at or near the Grímsvötn volcano, on the Vatnajökull glacier and in northeast Iceland, are described and analyzed. In Section III, data processing methodologies and radar-retrieval techniques are discussed and applied to the Keflavík C-band weather radar. In Section IV, the radar retrievals, in terms of the distal tephra fallout maps, the total tephra mass, the height, and the intensity of the ash eruption, are compared with the collected data at the ground to assess a preliminary error budget of radar remote sensing of ash clouds. The last section, *i.e.*, Section V, is dedicated to conclusions and tracing future research and development perspectives.

II. GROUND DATA ANALYSIS

The subglacial Grímsvötn volcano is located in the southeastern part of Iceland, in the most active part of the volcanic zones of the island [9], [4], [14].

The eruption of the first week of November 2004 was phreatomagmatic (without lava flows): The erupted magma was fragmented into pyroclasts of millimeter to submillimeter size. The erupted material was partly deposited at the volcanic vents and partly carried into the atmosphere by a volcanic eruption plume. The eruption was relatively small with the main explosive phase, visible to the Keflavík radar lasting about 33 h [14]–[16]. It produced a rising plume which bent over due to southerly winds. Fallout of tephra from the plume was most intense close to the vent, and most of it fell within a 50-km distance. Smaller amounts were carried much further to the north and northeast, reaching the coast of Iceland [18].

The tephra was deposited in a geographically well-defined area (see Fig. 1) and subsequently covered by winter snow. This situation provided a unique opportunity for systematic sampling of the tephra fall deposit and, thus, for estimating the total mass and the volume of erupted material [18].

A. Ash Distal Fallout Fields and Size Spectra Estimation

Ground sampling of ash deposits and grain sizes took place in the summers of 2005 and 2006 [7], [16], [17]. On the basis of distance from the volcano, two dispersion areas have been defined [7]: 1) the inner region within 40 km from the volcanic vent (area within the Vatnajökull glacier), excluding the crater region between the caldera proximity and 2 km away from the crater itself, and 2) the outer region between 40 and 140 km from the Grímsvötn volcano.

Sampling and mass fallout measurements of the tephra were done at 110 locations, with 69 being outside the 2-km distance from the crater. The sampling was done as follows: 1) through snow coring and weighting of the sample, yielding results in kilograms per square meter; 2) in the vicinity of the crater, where tephra thickness mostly exceeded 20–30 cm, the thickness was measured in pits and in the many ice crevasses in the area; and 3) in the area north of Vatnajökull, the tephra that fell on a specified area was collected and weighted. The bulk density of the tephra was found by sampling the undisturbed tephra with a shallow corer of known volume, drying the sample and weighing it. The mass per unit area in the crater area was then found by multiplying thickness and density [7].

The coordinates of the sampling points have been provided with reference to ÍSNET93, which is the Icelandic reference topographic mapping system. According to this map datum, the Earth is modeled with the Geodetic Reference System 1980 ellipsoid, with a semimajor axis length of 6378.137 km and inverse flattening $1/f = 298.257222101$ (where f indicates the flattening, which is a parameter to measure how much the ellipsoid departs from spherical). In order to provide an easy georeferencing coordinate system, ÍSNET93 coordinates have been converted into unprojected samples expressed in latitude and longitude coordinates [19]. The locations of the 69 tephra ground samples are shown in Fig. 2, which shows the measured ground samples, the Keflavík radar, and the Grímsvötn volcano positions superimposed on a low-resolution Icelandic coastal line map.

Tephra grain size analysis has been carried out only for ten samples, collected along two major dispersion axes (see Fig. 2) and well reported and documented in [17]. According to standard measurements, analyzed dimensions range from -4ϕ to 4ϕ [with ϕ as the conventional geological unit that is equal to $\phi = -\log_2 D$, with D (in millimeters) as the equivolume particle diameter] with a sieving step of 0.5ϕ ; with reference to scanned samples, about 15%–30% of the total mass has a diameter smaller than 4ϕ . Particles finer than 4ϕ have been studied using a laser granulometer with a sensitivity range of grain size from 0.02 to 2000 μm [16]. Obtained ash size data have been stored in table format, and examples of the mass ratio histograms versus a given diameter are shown in Fig. 3 as a function of the sampling distance from the Grímsvötn volcano [17].

The grain size distribution is a sample-dependent parameter, defined as the ratio between the mass at a given ϕ and the total

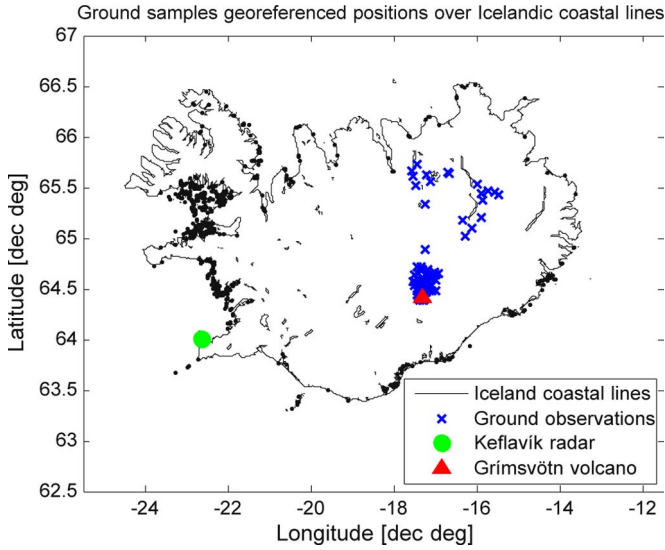


Fig. 2. Tephra-sample georeferenced locations over an Icelandic coastal line low-resolution map. (Crosses) All the processed 69 ground observations are shown, as well as (circle) the Keflavik radar and (triangle) the Grímsvötn volcano positions. Latitude and longitude are expressed in decimal degrees, with zero longitude at the Greenwich meridian (positive westward) and zero latitude at the equator parallel (positive northward). The black dots along the coastline are artifacts generated by the image representation at lower spatial resolution.

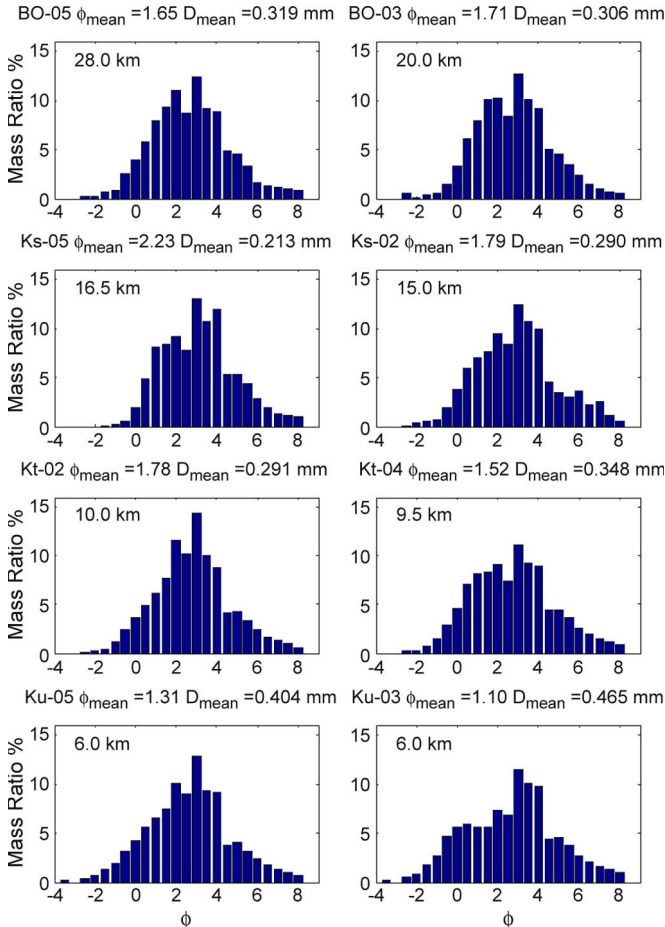


Fig. 3. Ash size distribution, with reference to some collected samples (BO-05, BO-03, Ks-05, Ks-02, Kt-02, Kt-04, Ku-05, and Ku-03) and to different distances from the Grímsvötn volcano (from 6 to 28 km; at the top—farther samples from the Grímsvötn volcano).

mass of the sample. These samples are collected at 6–30-km distance from the vent. Since more than 50% of the erupted material fell in the proximity of the vent, these samples cannot be used to determine the proportions of grain sizes produced in the eruption, but they indicate that there is no systematic change over this range of distances from the vent. They may therefore be a representative estimate of the grain sizes in the plume at medium distances.

The PSD suitably describes the occurrence per unit volume and per unit size of particles of a given diameter [20]. The PSD, usually expressed in $\text{m}^{-3}\text{mm}^{-1}$, is essential to estimate the radar backscattering and absorption properties of a volcanic cloud particle ensemble [12]. An iterative procedure to fit two theoretical PSD distributions, namely, scaled-gamma PSD (SG-PSD) and scaled-Weibull PSD (SW-PSD), has been performed in order to obtain the optimum values for shape parameters μ and γ . The formal expressions of SG-PSD (N_{SG}) and SW-PSD (N_{SW}) are [20], [12]

$$\begin{cases} N_{SG}(D; \mu, D_n, C_a) = N_{nG} \left(\frac{D}{D_n}\right)^\mu e^{-\Lambda_{nG} \left(\frac{D}{D_n}\right)} \\ N_{SW}(D; \mu, D_n, C_a) = N_{nW} \left(\frac{D}{D_n}\right)^\mu e^{-\Lambda_{nW} \left(\frac{D}{D_n}\right)^{\mu+1}} \end{cases} \quad (1)$$

where D is the equivolume particle diameter, D_n is the number-weighted mean diameter, N_{nx} and Λ_{nx} are the normalized PSD “intercept” and “slope” parameters (with $x = G$ or $x = W$), respectively, and C_a is the ash mass volumetric concentration. For the SW-PSD, $\mu = 3\gamma + 2$ holds, and sometimes, the parameter γ is preferred. The algorithm to fit the measured PSD $N_m(D)$, provided in terms of a sampled histogram, to the modeled PSD foresees the following steps [12].

- 1) Estimation of the ash particle mass concentration through the estimated third moment (\hat{m}_3) of PSD, once the ash density (ρ_a) is assumed, mass particle (m_a) is calculated, and minimum (D_1) and maximum (D_2) diameters are known:

$$\hat{C}_a \equiv \int_{D_1}^{D_2} m_a(D) N_a(D) dD = \frac{\pi}{6} \rho_a \hat{m}_3. \quad (2)$$

- 2) Estimation of the number-weighted mean diameter through the PSD estimated moments of zero order (\hat{m}_0) and first order (\hat{m}_1)

$$\hat{D}_n = \frac{\int_{D_1}^{D_2} D N_a(D) dD}{\int_{D_1}^{D_2} N_a(D) dD} = \frac{\hat{m}_1}{\hat{m}_0}. \quad (3)$$

- 3) Computation of the PSD “intercept” and “slope” parameters N_{nx} and Λ_{nx} from estimated C_a and D_n at previous steps with the method of moments.
- 4) Minimization of the sum of squared differences between the measured PSD $N_m(D)$ and the model ones $N_{Sx}(D)$ in order to estimate the shape parameter μ (or γ)

$$\hat{\mu} = \text{Min}_\mu \left\langle \left[\sum_{i=1}^{N_D} \left(N_{Sx}(D_i; \mu, \hat{D}_n, \hat{C}_a) - N_m(D_i) \right) \right]^2 \right\rangle \quad (4)$$

where D_i denotes the discrete sampled diameters, N_D is the total number of diameters in which the PSD is

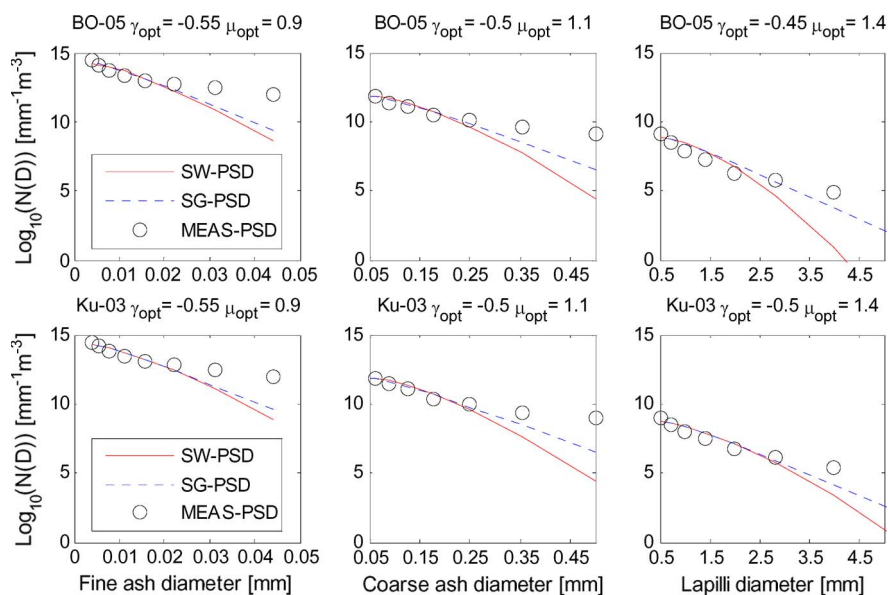


Fig. 4. Graphic view of the best fitting results: (SG-PSD) scaled-Gamma function and (SW-PSD) scaled-Weibull function fitted to (MEAS-PSD) the measured PSDs of BO-05 and Ku-03 samples, with reference to three diameter classes (fine ash, coarse ash, and lapilli). Computed values of γ_{opt} and μ_{opt} are also quoted.

partitioned, and “ $\langle \cdot \rangle$ ” indicates the ensemble average over the PSD available measurements.

With reference to SG-PSD, the searched shape parameter μ ranges from 0 to 6 with a step of 0.1, whereas for SW-PSD, the shape parameter γ ranges from -0.9 to 0 with a step of 0.05 . Three optimum values of shape parameter have been obtained for each sample, because the algorithm has been applied to all ten available samples according to the following diameter classification: fine ashes with an average $\langle D_n \rangle = 0.006$ mm and a variability $0.001 \leq D_n \leq 0.06$ mm, coarse ash with $\langle D_n \rangle = 0.064$ mm and $0.06 \leq D_n \leq 0.5$ mm, and lapilli with $\langle D_n \rangle = 0.583$ mm and $0.5 \leq D_n \leq 7.0$ mm.

For each class, the optimum value of the shape parameter has been computed by means of a simple arithmetic mean among the ten available samples, obtaining $\mu_{opt} = [0.9 \ 1.1 \ 1.4]$ and $\gamma_{opt} = [-0.55 \ -0.50 \ -0.45]$. Graphical results of the best fitting of SG-PSD and that of SW-PSD to the measured samples (black circles) are shown in Fig. 4. It is worth noting that the SG-PSD and SW-PSD show similar results for diameters smaller than 0.064 mm, whereas SG-PSD shows a better fit to the measurements than SW-PSD for bigger diameters.

It is worth mentioning that, in our analysis, we are implicitly assuming that PSDs derived from ground deposits resemble that in the air, an assumption being verified only in the case of uniform vertical distribution of ash PSD and the absence of gravitational settling. Indeed, the use of a particle disdrometer (also called spectrometer) might give a real-time ash size distribution either close to the ground (if they are based on microwave Doppler measurements) or on the ground (if they are based on optical imaging) [24]. The only way to truly assess the nature of airborne PSD would be a direct flight through the ash cloud, an effort which is highly risky even when using unmanned airborne vehicles.

B. Ash Fallout Mass and Volume Ground Sampling

The volume and the mass of tephra fall deposits are important parameters in establishing the magnitudes of eruptions and in

assessing risk and vulnerability [4], [21]. In many cases, data sets are incomplete, making the estimation of volume far from being straightforward. A variety of methods have been used to calculate deposit volumes, e.g., [21]–[26]. All of these methods are empirical and based on thickness measurements of tephra.

Ground mass loading or ash depth $D_s(x, y)$ (in kilograms per square meter) at the location (x, y) is derived directly from the weight of the dried tephra in the snow cores obtained *in situ* in the 5–50 km distance range. In the proximal area, within 3–4 km from the vents, the ground mass loading values were computed by taking into account the spatially dependent ash density $\rho_a(x, y)$ and the measured depth $h_s(x, y)$ of the accumulated ash as follows:

$$D_s(x, y) \cong \rho_a(x, y) h_s(x, y) \quad (5)$$

where h_s is expressed in meters and ρ_a is in kilograms per cubic meter. In the region north of Vatnajökull, the ground mass loading was obtained directly by collecting the tephra from a specified area and weighing it.

Distal ash fallout mass loading values D_s are shown in Fig. 5, where the samples have been interpolated over the area referring to the northeastern region of the Vatnajökull glacier using the nearest neighbor method. In this figure, the interpolated map shows a minimum value of 0.01 kg/m², indicating that presumably lower values can be found within farther areas in the northeastern Icelandic coast. Moreover, areas with a mass loading of 0.5 kg/m² enclose about 93% of the overall ash in an area of approximately 1465 km². Moving away from the volcano, the ash loading roughly falls off: the area with a mass loading of 40 kg/m² (equivalent to ~ 3.5 -cm-thick layer of tephra) is within 77 km² from the caldera, the area with a loading of 10 kg/m² extends over an area of 156 km² northward the volcano, and the area with a loading of 5 kg/m², which looks considerably more dispersed on the ground, is within 423 km².

In the case of the Grímsvötn eruption, the material erupted is divided between the ice cauldron around the craters, where ice

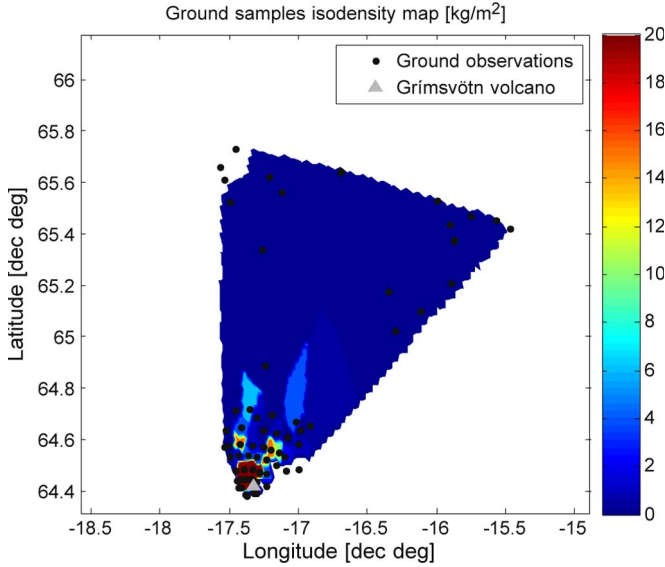


Fig. 5. Tephra georeferenced distal fallout field near the volcano region and around Vatnajökull glacier, gathered from sampling data processing. The isomass lines are expressed in kilograms per square meter and have been obtained through a nearest neighbor interpolation on sample data; ground samples are represented by black dots, whereas the Grímsvötn volcano is symbolized by the gray triangle. The reference system is the same as in Fig. 2.

cap melted out due to the volcanic heat, and the region outside the cauldron. Surveys in 2005–2006 showed that the thickness of the tephra in the 500 m by 750 m elliptically shaped cauldron was about 70 m and the volume was $2.3 \pm 0.4 \cdot 10^7 \text{ m}^3$. Using the tephra density of $\rho_{a0} = 1200 \text{ kg/m}^3$, and $h_I = 70 \text{ m}$, the total mass of the material contained within the cauldron M_{sI} is estimated to be around $2.7 \pm 0.5 \cdot 10^{10} \text{ kg}$ [16].

The sample total mass M_{sO} of the tephra fallout outside the ice cauldron is computed by integrating the mass loading map over the outer region as follows:

$$M_{sO} = \int_{D_s \geq D_{\min}} D_s(x, y) dS \quad (6)$$

where $D_s(x, y)$ is the deposited tephra mass loading within the interpolation grid, identified by the condition $D_s > D_{\min}$ with $D_{\min} = 0.1 \text{ kg/m}^2$, and dS (in square meters) is the resolution area of the interpolated grid. From [17], $D_s(x, y)$ has been obtained from point samples using a kriging spatial interpolation method, thus obtaining, using (6), $M_{sO} = 2.7 \pm 0.5 \cdot 10^{10} \text{ kg}$. In addition, $0.2 \cdot 10^{10} \text{ kg}$ is estimated to have fallen outside the $D_{\min} = 0.1 \text{ kg/m}^2$ so that this term must be added to M_{sO} , leading to $M_{sO} = 2.9 \pm 0.5 \cdot 10^{10} \text{ kg}$.

Therefore, the sampled total mass M_{sT} of erupted material is the sum of two inner and outer contributions

$$M_{sT} = M_{sI} + M_{sO} \cong \rho_{a0} V_{sT} \quad (7)$$

obtaining a value $M_{sT} = 5.6 \pm 1.0 \cdot 10^{10} \text{ kg}$. The sample tephra total volume is then given by the last term of (7), where $V_{sT} = V_{sI} + V_{sO}$ (in cubic meters) is the sum of the inner (ice cauldron) and outer material volumes. The following values have been estimated: $V_{sI} = 2.3 \pm 0.5 \cdot 10^7 \text{ m}^3$ and $V_{sO} = 2.4 \pm$

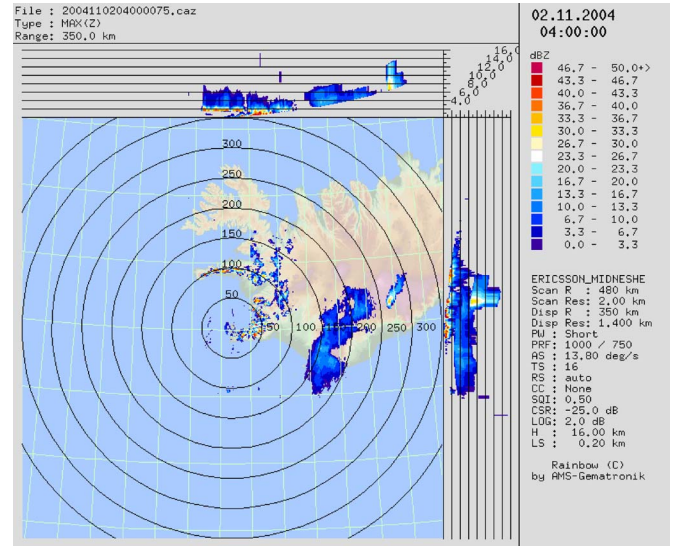


Fig. 6. HVMI radar image at 04:00 UTC on November 2, 2004, using Rainbow software and showing the recorded Keflavík C-band radar reflectivity, whose maximum values are projected on the surface as (bottom-left panel) a PPI radial map and projected on (top and right side of the HVMI image) two orthogonal planes along the vertical. The eruption plume is visible over Grímsvötn in the map at altitudes above 6 km and radial distances larger than 250 km. The upper graph shows the north–south profile of the plume, while the graph to the right shows the east–west profile. Note that the uncorrected ground clutter returns from ranges less than 200 km.

$0.4 \cdot 10^7 \text{ m}^3$, thus resulting to $V_{sT} = 4.7 \pm 0.9 \cdot 10^7 \text{ m}^3$, as documented in [16].

There are at least two approximation error sources in computing D_s : the first one is related to the sampling error (error in corer diameter and weighted mass) and to the random error that depends on the uncertainty in how representative the sample is, whereas the second depends on uncertainty in the interpolation method. From [17], the first error typology, expressed in relative terms, is virtually negligible (less than 1%), whereas the sampling error amounts to 5% and the random error, which is not easy to compute, is assumed to be equal to 10%. With respect to the second contribution, an uncertainty of 15% has been assumed when generating isomass loading maps through kriging interpolation. Therefore, the most probable error is equal to the quadratic sum of the aforementioned contributions and amounts to about 19%.

III. RADAR DATA PROCESSING

The eruption was detected and monitored during its whole life span by the C-band (6-GHz) weather radar in Keflavík, located 260 km west of the Grímsvötn volcano's caldera, as shown by the horizontal vertical maximum indicator (HVMI) recorded radar image shown in Fig. 6. The Keflavík C-band radar volumes were available from the Icelandic Meteorological Office every 5 min from 21:20 Coordinated Universal Time (UTC) on November 1, 2004, until 09:55 UTC on November 3, 2004. The radar data set consists of 440 volumes in spherical coordinates with 10 elevation angles, 360 azimuth angles, and 240 range bins, the latter having a width of about 2 km [13]. The analysis of the radar imagery and its processing is described in [7] and [13] so that only modifications to that approach will be described here.

Weather radar systems, although designed to study hydrometeors and rain clouds, can be used to monitor and measure volcanic eruption parameters. Both radar targets have the same measuring principle: both rain clouds and ash clouds feature quite similar fragmentation and aggregation processes and can cause backscattering and absorption of incident radiation, transmitted by the radar. The measured radar backscattered power is proportional to the copolar horizontally polarized reflectivity factor (Z_H), which, in the Rayleigh condition, is expressed by [11]

$$Z_H = \int_{D_1}^{D_2} D^6 N_{Sx}(D) dD = m_6 \quad (8)$$

where m_6 is the sixth PSD moment, D (in millimeters) is the equivolume particle diameter, and N_{Sx} is the PSD model as in (1), where $x = G$ or $x = W$ stands for SG-PSD or SW-PSD, respectively. From (8), it is noted that, keeping the ash particle amount constant, the reflectivity factor Z_H is higher for bigger particles. If the PSD is known and assuming spherical particles with a given composition and dielectric properties, then (8) allows one to simulate the Rayleigh response of a weather radar.

The weather radar response is mainly controlled by the PSD within the range volume bin. In the case of ash cloud formation processes within a humid environment, we may suppose to have two distinct particles-combination phenomena within an observed range volume: 1) coexistence of ash particle and hydrometeors without mixing processes and 2) aggregation (or mixture) of ash particles with hydrometeors to form a new mixed-phase particle [6], [20]. Coexistence and mixture of ash particles with cloud ice and water droplet generally lead to a reduction of the measured reflectivity up to 5–10 dBZ for a fractional combination of about 50% [13]. The use of single-polarization weather radar and the absence of ancillary data may prevent the discrimination between ash, hydrometeors, and mixed particles since their horizontally polarized reflectivity response is quite similar and the effect of their shape and composition is generally unknown. It is worth noting that the same uncertainty affects the satellite-based estimates of ash loading [10].

A. VARR

The VARR approach utilizes two steps: 1) ash classification and 2) ash estimation [7]. Both steps are trained by a physical-electromagnetic forward model, summarized by (8), where the main PSD parameters are supposed to be constrained random variables. The generation of a simulated ash-reflectivity data set by letting PSD parameters to vary in a random way can be framed within the so-called Monte Carlo techniques.

Automatic discrimination of ash classes with respect to size (fine, coarse, and lapilli) and concentrations (small, moderate, and intense) implies the capability of classifying the radar volume reflectivity measurements into one of the nine mentioned classes. Once the ash class is discriminated, then the ash concentration and fallout can be estimated by statistical techniques using the same training simulated data sets. Within the VARR technique, ash classification is performed by the

use of maximum *a posteriori* (MAP probability) estimation. The probability density function (pdf) of each ash class (c), conditioned to the measured reflectivity factor (Z_{Hm}), can be expressed by Bayes theorem. The MAP estimation of ash class c corresponds to the maximization with respect to c of the posterior pdf $p(c|Z_{Hm})$. Under the assumption of multivariate Gaussian pdfs, the previous maximization reduces to the following minimization [7]:

$$\hat{c} = \text{Min}_c \left[\frac{\left(Z_{Hm} - m_Z^{(c)} \right)^2}{\left(\sigma_Z^{(c)} \right)^2} + \ln \left(\sigma_Z^{(c)} \right)^2 - 2 \ln p(c) \right] \quad (9)$$

where Min_c is the minimum value with respect to c , $m_Z^{(c)}$ and $\sigma_Z^{(c)}$ are the reflectivity mean and standard deviation of class c , and $p(c)$ is the *a priori* pdf of class c , and the ash class perturbations have been assumed uncorrelated. Computing (9) requires knowledge of the reflectivity mean ($m_Z^{(c)}$) and standard deviation ($\sigma_Z^{(c)}$) of each ash class c . This statistical characterization of each cloud class can be derived from a simulated synthetic data set where PSD may be either arbitrarily defined or experimentally measured.

Aside from ash concentration C_a given in (2), VARR can also retrieve, for each radar range bin, the ash fallout rate (R_a) (in kilograms per square meter per second), defined as the mass crossing a horizontal section per unit area in a given time interval, expressed by

$$\hat{R}_a \equiv \int_{D_2}^{D_1} v_a(D) m_a(D) N_a(D) dD = \frac{\pi}{6} a_v \rho_a m_{3+b_v} \quad (10)$$

where $v_a(D)$ is the terminal ashfall velocity in still air when the vertical component of the air speed is neglected and m_a and N_a are the actual ash mass particle and its size distribution. The right-hand side of (10) is obtained after assuming a power law for v_a dependence on D , i.e., $v_a(D) = a_v D^{b_v}$ with a_v and b_v as empirical coefficients. The latter are given, in our case, by two different empirical models: $a_v = 5.558$ [m/s] and $b_v = 0.722$ as in [4] and $a_v = 7.460$ [m/s] and $b_v = 1.0$ for 5–10-km heights as in [36].

Through the training forward model in (8), a regressive approximation of (2) and (10) may be used as a function of the class c which is discriminated by the ash size and concentration [7]

$$\begin{cases} C_a^{(c)} = a_c Z_{Hm}^{b_c} \\ R_a^{(c)} = c_c Z_{Hm}^{d_c} \end{cases} \quad (11)$$

In (11), the regression coefficients a_c , b_c , c_c , and d_c are obtained assuming zero-mean random noise on the copolar reflectivity due to instrumental and forward modeling uncertainties; the measured copolar reflectivity Z_{Hm} is simulated by assuming that the estimated coefficient of variation of R_a is about 10%. As already mentioned, we can take into account the effect of aggregation between ash and hydrometeors as a further uncertainty within the modeled noise [20]. This is a conservative choice, but it is the only way to introduce this

knowledge within our inversion algorithm, apart from possible *a priori* meteorological information. The modeled noise is added to simulated reflectivity Z_H of pure ash to reproduce the synthetic reflectivity measurement signatures Z_{Hm} [13].

B. Ash Mass, Density, and Volume Radar Retrieval

The VARR technique can be applied to each radar resolution volume in 3-D spherical coordinates where the C-band measured reflectivity factor Z_{Hm} is larger than the minimum detectable reflectivity (MDZ). The latter has been obtained from the Keflavík radar specifications; at a range of about 260 km, MDZ is about -3 dBZ. Indeed, only plain position indicators (PPIs) at the first five available elevation angles have been used, as the other ones were useless since radar beam heights did not intercept the ash plume at higher elevations (see Fig. 6). Raw reflectivity data were averaged to about 2-km radial resolution in order to enhance the signal-to-noise ratio and thus reduce the MDZ. The VARR products in terms of ash concentration C_a and fallout R_a are originally provided within 3-D spherical coordinate (r, φ, θ) reference system. From the inversion of the “haversine” formula, used to compute the great-circle distance (i.e., the shortest distance over the surface of the Earth) between two points, and supposing the International Standard Atmosphere for electromagnetic wave propagation [38], [39], (r, φ, θ) has been converted into longitude, latitude, and terrain altitude (lon, lat, alt) to be able to geolocate radar returns [11]. A finer grid (x, y, z) has been generated from (lon, lat, alt) in order to virtually increase the spatial resolution of data.

The instantaneous volcanic ash cloud volume $V_a(t)$ (in cubic meters), which represents the volume of the ash cloud at a given time step t (the latter is referred to as “instantaneous” even though the radar employs about 2 min to complete a volume scan), may be estimated by using a threshold (C_{ath}) on the estimated concentration $C_a(x, y, z; t)$ at a given position (x, y, z) as follows:

$$V_a(t) \equiv \int_{C_a(x,y,z;t) \geq C_{ath}} dV \quad (12)$$

where dV (in cubic meters) is the elementary volume ($dV = dx dy dz$). The radar-derived total volume can then be computed by

$$V_{aT} \equiv \int_{t_i}^{t_f} V_a(t) dt \quad (13)$$

where t_i and t_f are the initial and final time steps of the volcanic eruption.

The instantaneous volume $V_a(t)$ in (12) should be, indeed, distinguished into the real detected volume $V_{ad}(t)$ and an undetected (hidden) portion $V_{ah}(t)$. In general, $V_a(t) = V_{ad}(t) + V_{ah}(t)$ due to the radar observation geometry, the presence of occlusions along the ray paths, and the presence or not of ash in the atmosphere; the term V_{ah} implies that the total portion of the ash cloud $V_a(t)$ may not be detected by the scanning radar, thus inducing an underestimation of the total ash volume and mass. This problem, which is clearly visible in Fig. 6 by looking

at the horizontal and vertical projections and is worse at larger distances, is a well-known problem in radar meteorology, and it is often overcome relying on the reconstruction of the vertical profile of reflectivity (VPR) [33].

An approximate way to approach the VPR problem is to project the measured reflectivity Z_{Hm} , available at the lowest range bin, down to the terrain height at $z = z_s$. This VPR model assumes that the lowest detectable backscattering value is the major contributor of ash fallout, deposited on the ground from the vertical column above a considered position. To some extent, this approach is similar to that adopted when estimating the total mass from satellite thermal-infrared radiometers when estimates of ash cloud top layers are extrapolated to ground (e.g., [10]). An alternative way is to assume the precipitating ash fallout to be equal to the maximum Z_{Hm} on the same vertical column. In both approaches, we are neglecting the finite time interval that a radar resolution volume (bin) of ash takes to reach the ground (given an ash terminal velocity); the latter, coupled with the horizontal transport effects, may cause a displacement between the radar measure and the actual ash deposition on the ground.

The spatial distribution of the instantaneous maximum plume height $H_a(x, y; t)$ (in kilometers) can then be derived by using either a threshold (Z_{Hmth}) on the measured reflectivity $Z_{Hm}(x, y, z; t)$ or a threshold (C_{ath}) on $C_a(x, y, z; t)$ as in (12)

$$H_a(x, y; t) \equiv \begin{cases} \text{Max}_z \{z | Z_{Hm}(x, y, z; t) \geq Z_{Hmth}\} \\ \text{Max}_z \{z | C_a(x, y, z; t) \geq C_{ath}\} \end{cases} \quad (14)$$

where Max_z is the maximum operator with respect to z . The two approaches are not necessarily providing the same result, as will be shown in the next section. The maximum height H_{aM} of $H_a(x, y; t)$ with respect to the position (x, y) in (14) provides a single geometrical product for each radar volume scan

$$H_{aM}(t) \equiv \text{Max}_{x,y} \{H_a(x, y; t)\} \quad (15)$$

where $\text{Max}_{x,y}$ is the maximum operator with respect to (x, y) . The maximum height H_{aM} can be also referred to the spatial subdomain around the volcano vent [34]. It is worth noting that the degraded radial resolution (about 2 km in our case) may be erroneously considered a minimum step for estimating H_a or H_{aM} . Indeed, the radar radial resolution coincides with the vertical resolution only for antenna zenithal pointing (or elevation angle equal to 90°). For low elevation angles, such as those of scanning weather radars (in our case, the suitable elevations are 0.5° , 0.9° , 1.3° , 2.4° , and 3.5°), the vertical coordinate z is resolved at a variable range-dependent resolution which, in our case, may be even less than a few hundreds of meters [13].

The instantaneous ash mass $M_a(t)$ (in kilograms) from each radar 3-D volume V_a is given by

$$M_a(t) \equiv \int_{V_a} C_a(x, y, z; t) dV \quad (16)$$

where (x, y, z) are the longitude, latitude, and altitude coordinates within the considered region. Similar to M_a , the

instantaneous spatial distribution of the ash vertically integrated columnar content $I_a(x, y; t)$ (in kilograms per square meter), which is the total ash within a vertical column of height H_a , can be estimated through the estimated C_a as

$$I_a(x, y; t) \equiv \int_{H_{aM}(x, y, t)} C_a(x, y, z; t) dz \quad (17)$$

where $H_{aM}(x, y; t)$ is the plume maximum height and the region (x, y) may be arbitrarily chosen around the vent.

The deposited ash on the ground during the whole event can be estimated from the retrieved ashfall rate $R_a(x, y, z, t)$ (in $\text{kg/m}^2 \cdot \text{s}$). By performing a VPR reconstruction as indicated before and indicating with $R_a(x, y, z = z_s, t)$, the ashfall rate at the surface height z_s , the spatial distribution of the radar-derived deposited tephra mass loading $D_a(x, y)$ is obtained from

$$D_a(x, y) \equiv \int_{t_i}^{t_f} R_a(x, y, z = z_s, t) dt \quad (18)$$

where t_i and t_f are the initial and final time steps of the volcanic eruption. The surface depth $h_a(x, y)$ (in meters) of the accumulated ash in a given position can then be estimated by knowing the spatially dependent ash density $\rho_a(x, y)$, as in (5), through

$$h_a(x, y) \cong D_a(x, y) / \rho_a(x, y). \quad (19)$$

In a way similar to ground sampling procedure, we can evaluate the total space–time deposited tephra from radar measurements by using

$$M_{aT} = \int_{D_a \geq D_{\min}} D_a(x, y) dS \cong V_{aT} \rho_{a0} \quad (20)$$

where V_{aT} is the radar-derived total ash volume, defined in (13), and ρ_{a0} is the average ash density. From (20), the total eruption ash volume V_{aT} (in cubic meters) is obtained from $V_{aT} = M_{aT} / \rho_{a0}$.

Indeed, the radar samples are sorted using discrete time and space steps. Thus, the deposited tephra mass loading $D_a(x, y)$ in (18) as well as the quantities in (13), (16), and (17) require the knowledge of the spatial and temporal resolutions of the data. For what concerns the spatial resolution, the radial resolution is constant (here, reduced to about 2 km), whereas the transverse resolution quadratically increases with the radar range. Temporal resolution is usually constant (here, about 5 min), and it can be used to practically compute the tephra mass loading $D_a(x, y)$ in (18) by considering the N_r radar volume scan temporal samples with Δt_r as the sampling time interval.

C. Ash Cloud Tracking From Radar Imagery

Wind effects on the ash cloud shape may play a relevant role in determining the tephra dispersion. Ground wind data from weather station were not available near the eruption vent,

whereas only synoptic radio soundings were delivered every 12 h in Keflavík near the radar site.

Within this framework, we have decided to extract the plume transport information using the time series of the ash ground concentration maps $D_a(x, y)$ (in kilograms per square meter) acquired every 5 min. A time–space correlation technique, named phase correlation (PCORR) [27], has been used for this purpose. PCORR is based on the comparison between two subsequent digital images to compute the displacement field. The foreseen estimation of the displacement field in its horizontal and vertical motion vector components $u = U(x, y)$ and $v = V(x, y)$, respectively, is then obtained by a Lagrangian persistence scheme

$$D_a(x, y, t_0 + n \cdot \Delta t) = D_a(x - u \cdot n \cdot \Delta t, y - v \cdot n \cdot \Delta t, t_0) \quad (21)$$

where Δt is the sampling time, t_0 is the instant, and (x, y) is the position where the nowcasting procedure starts and n (integer number) drives the number of forecasted maps. When U and V are set to zero in (21), the special case of the Eulerian persistence is obtained; when U and V are chosen constant over the considered space domain, instead, we get the so-called steady-state displacement (SSD). In this case, owing to the 5-min sampling, an SSD approach resulted in a quite good assumption. Assuming two subsequent maps of the same size (i.e., both of them with N rows and M columns), D_a at time t_1 , and D'_a at time t_2 , the spatial cross-correlation function F_{RR} is expressed by

$$F_{RR}(\Delta x, \Delta y) = \int \int D_a(x, y) \cdot D_a'^*(x - \Delta x, y - \Delta y) dx dy \quad (22)$$

where $(\Delta x, \Delta y)$ indicates the Cartesian displacement along the x - and y -axes, $D_a(x, y)$ indicates the ash ground concentration D_a of the first image at pixel (x, y) , the symbol “ $*$ ” is the complex conjugate operator, and the integral is extended over the area where D_a and $D_a'^*$ overlap. F_{RR} measures the statistical correlation between two samples $D_a(x, y)$ and $D'_a(x, y)$ for a given shift $(\Delta x, \Delta y)$; the identification of the place of the maximum of F_{RR} corresponds to the shift inside a query window. The whole available pairs of maps have been used, thus implementing the SSD method applying a single motion vector to compute the advected field.

The high computational cost of PCORR has been reduced by operating in the frequency domain, given the Fourier shift theorem which states that a spatial lag $(\Delta x, \Delta y)$ of a signal is equivalent to a phase change in the spatial frequency domain (k_x, k_y) . The frequency-domain approach also overcomes problems regarding wrong motion directions and magnitude computation caused by the saturation effect in proximity of the correlation function multiple maxima. Therefore, the bidimensional cross correlation in (22) can be rewritten as follows:

$$F_{RR}(\Delta x, \Delta y) = \mathfrak{F}^{-1} \left\{ \mathfrak{F} [D_a(k_x, k_y)] \cdot \mathfrak{F} [D_a'^*(k_x, k_y)] \cdot e^{j2\pi(k_x \Delta x + k_y \Delta y)} \right\} \quad (23)$$

where $D'_a = D_a(x - \Delta x, y - \Delta y)$ and \mathfrak{F} is the discrete Fourier transform that has been applied by means of the fast

Fourier transform algorithm. The displacement components Δx and Δy , supposed to be the sole responsible of the displacements between D_a and D'_a , are only accounted by the exponential term in (23). This suggests to suppress the modulus of the exponential term, deriving the following expression:

$$\begin{aligned} P_{RR}(\Delta x, \Delta y) &= \mathfrak{S}^{-1} \left\{ \frac{\mathfrak{S}[D_a(k_x, k_y)] \cdot \mathfrak{S}[D'_a(k_x, k_y)] \cdot e^{j2\pi(k_x \Delta x + k_y \Delta y)}}{\mathfrak{S}[D_a(k_x, k_y)] \cdot \mathfrak{S}[D'_a(k_x, k_y)]} \right\} \\ &= \mathfrak{S}^{-1} \left\{ e^{j2\pi(k_x \Delta x + k_y \Delta y)} \right\} = \delta(x - \Delta x, y - \Delta y). \quad (24) \end{aligned}$$

The last equation in (24) defines the PCORR method which produces as output a Dirac function δ , centered on the searched displacements $(\Delta x, \Delta y)$. The Dirac function holds only if the displacement is purely linear or, in other words, no rotational components contribute to the motion; when rotational components are present, spurious contributions arise near the maximum as noise.

The application of the PCORR technique to radar products consists of comparing two radar product images, derived from the scan volume, to obtain the time evolution of the ash estimate spatial distribution, taking into account wind transport effects. There are two main steps: 1) image analysis, to define the shift field in the form of vectors, and 2) image modification, based on the information given by the use of the PCORR technique. Using this technique, two ash ground concentration subsequent images (at times t and $t + \Delta t$, with Δt equal to 5 min) have been processed in order to generate interpolated images with a synthetic sampling time of 60 s between each couple of PPI images, thus obtaining an overall number of distribution images five times bigger than the scan number. In order to assess the goodness of the advection method, a comparison between the advected radar image and its corresponding acquisition at the same time has been carried out on the whole event. The correlation coefficient has been taken into account to accomplish the aforementioned comparison. A quality check of the time series radar maps has been performed to avoid the inclusion of nonsignificant levels of ash concentration within the comparison. In particular, a threshold of 1% on the ratio between non-zero concentrations, with respect to the overall concentration of the ash distribution within a spatial map, has been fixed. The obtained mean value of the correlation coefficient is about 0.593, which is comparable to typical values reported in the literature for meteorological clouds [35].

D. VARR Processing Techniques

In order to perform a sensitivity analysis to different processing choices, the VARR technique is distinguished in this work among three basic versions:

- 1) VARR_D, indicating the default (subscript D) VARR approach with PSD of nine classes c arbitrarily set up as in [7] and [13];
- 2) VARR_C, indicating the VARR_D calibrated (subscript C) algorithm when PSD is trained on ash size samples collected from the ground. Depending on the ground

projected vertical column data, two versions have been implemented:

- a) VARR_{CL} denotes the VARR_C where the precipitating ash fallout is assumed equal to the lowest (subscript L) detectable value.
- b) VARR_{CM} indicates the VARR_C version where the precipitating ash fallout is assumed equal to the maximum (subscript M) on the vertical column.
- 3) VARR_{CLS}, indicating the VARR_{CL} where the ash size (subscript S) is taken into account, in the sense that only coarse ash and lapilli are considered as falling to the ground.

The VARR_C algorithm has been implemented by appropriately modifying the VARR_D version to fit the algorithm to the Grímsvötn volcano eruption, considering the results of the ground sampling. Nominal values of the diameter mean weight number with reference to the three introduced ash classes (fine, coarse, and lapilli) have been obtained by collected sample grain size and measured PSD, as shown in Section II-A. Optimal values of shape parameters have been adopted through the best fitting of SG-PSD and SW-PSD to the measured PSD with reference to each fixed diameter class (note that, in VARR_D, only one shape parameter, obtained from the eruptions of other volcanoes, is used to compute the PSD trend). Through ground sampling of six sections on the rim of the ice cauldron formed during the eruption, the mean ash density of dried samples has been estimated as 1200 kg/m³ (instead of 1000 kg/m³, which is the value used in VARR_D).

The VARR_{CLS} exploits the ash classification procedure in order to consider fine ash particles as nonprecipitating. A label c [see (9)], ranging from 1 to 9, has been attached to each radar resolution volume, where the values correspond to the different ash-size–ash-concentration combinations [7], [13]: 1 for fine ash with small concentration, 2 for fine ash with moderate concentration, 3 for fine ash with intense concentration, 4 for coarse ash with small concentration, 5 for coarse ash with moderate concentration, 6 for coarse ash with intense concentration, 7 for lapilli with small concentration, 8 for lapilli with moderate concentration, and 9 for lapilli with intense concentration. The 0 has been assigned to nonsignificant radar volumes (i.e., volumes where the reflectivity factor was undistinguishable from the background noise).

The tephra ground distribution considering the wind transport effects should be also considered when comparing ash distal deposits derived from radar scans. In the following, we will indicate the application of PCORR technique to VARR, introducing the subscript “A” to the considered VARR option (e.g., advected VARR_C is indicated by VARR_{CA}). This means that VARR_{XA} differs from VARR_X since it tends to release ash mass at a ground position which is shifted with respect to the position along the vertical column of the considered range bin. The impact of using VARR_{XA}, instead of VARR_X, is expected to be significant, particularly when considering the spatial distribution of distal ash.

IV. DATA INTERCOMPARISON

The results of the VARR algorithm in its various options, applied to radar data gathered during the Grímsvötn volcano

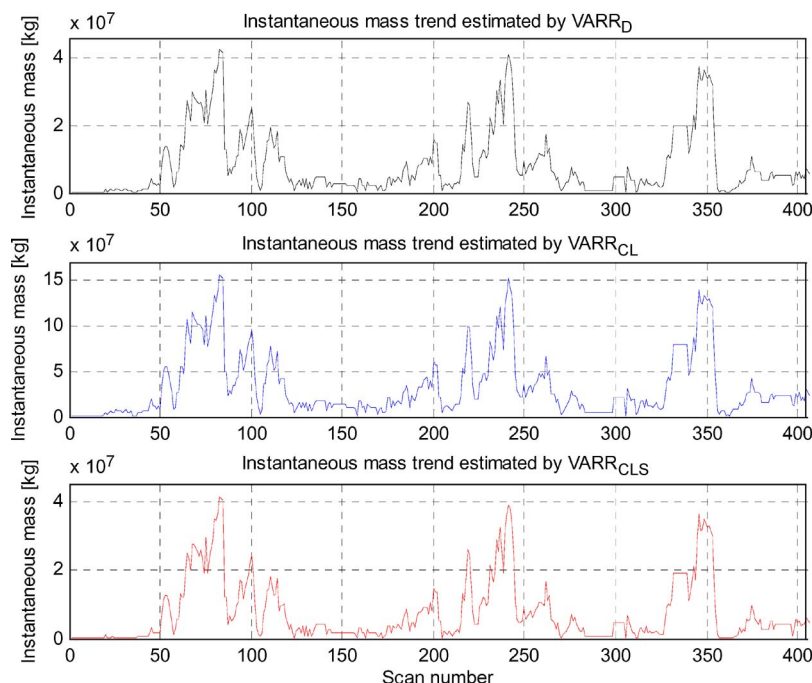


Fig. 7. Instantaneous mass (obtained from ash rate R_a) versus time expressed in terms of scan number for VARR_D, VARR_{CL}, and VARR_{CLS}. The scan sampling period is equal to 5 min, so that the time series shows a time window of about 2190 min (equal to 36.5 h) since the first available radar data at 21:20 UTC on November 1, 2004.

eruption, are illustrated and discussed in the following paragraphs by considering the following parameters of volcanological interest: mass concentration, maximum height of the ash cloud, total mass and volume, eruption discharge rate (EDR), and spatial ash distribution by means of PCORR technique. Results are quantitatively compared with deposited ash ground sampling [17].

A. Distal Ash Fallout Maps

Distal fallout maps have been obtained with reference to five different VARR algorithm options, as already discussed: VARR_D indicating the “default” VARR approach, VARR_{CL} indicating the “calibrated with last column value” VARR approach using measured PSDs, VARR_{CM} indicating the “calibrated with maximum column value” VARR approach using measured PSDs, VARR_{CLA} indicating the “calibrated with last column value and advected” VARR approach, and VARR_{CLS} indicating the “calibrated with last column value and ash size discrimination” VARR approach.

The temporal trend of the instantaneous total mass $M_a(t)$, retrieved from the scanning radar and defined in (16), is shown in Fig. 7 with reference to VARR_D, VARR_{CL}, and VARR_{CLS} techniques. These plots are useful to estimate the intensity of the volcanic eruption in near real-time mode. The scan sampling period is equal to 5 min so that the time series shows a time window of about 2190 min (equal to 36.5 h) since the first available radar measurements at 21:20 UTC on November 1, 2004. Fig. 7 clearly shows a pulsing behavior of the eruption with three main pulses, where the time between peaks in plume mass was 8 and 12.5 h. The application of the different VARR techniques leads to different results, with an instantaneous mass M_a larger (by about four times) for VARR_{CL} than for VARR_D and VARR_{CLS}, as expected. When the lowest detectable radar

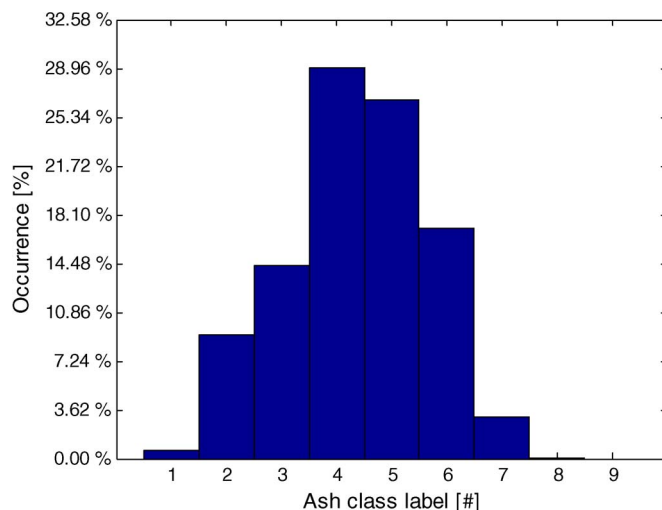


Fig. 8. Histogram of the estimated ash classes by using VARR_{CLS} during the whole eruption event detected by the Keflavik C-band radar (440 scan volumes). The class labels correspond to 0 = Background noise, 1 = Fine ash/small concentration, 2 = Fine ash/moderate concentration, 3 = Fine ash/intense concentration, 4 = Coarse ash/small concentration, 5 = Coarse ash/moderate concentration, 6 = Coarse ash/intense concentration, 7 = Lapilli/small concentration, 8 = Lapilli/moderate concentration, and 9 = Lapilli/intense concentration. Note that class 9 has not been detected during this event, whereas class 0 has been excluded; the total number of ash-detected volume bins is 27 621 (within a total of 4 787 200 acquired bins).

bins are considered, the PSD calibration of VARR provides an ash mass bigger than that estimated from VARR_D.

The comparison between VARR_{CL} and VARR_{CLS} in Fig. 7 also shows that the sensitivity to the ash category is quite relevant in the radar mass estimation. The latter consideration is confirmed by Fig. 8, which shows the histogram of the nine radar-estimated ash categories by VARR_{CLS} during the whole eruption event. Note that the total available 4 787 200 radar

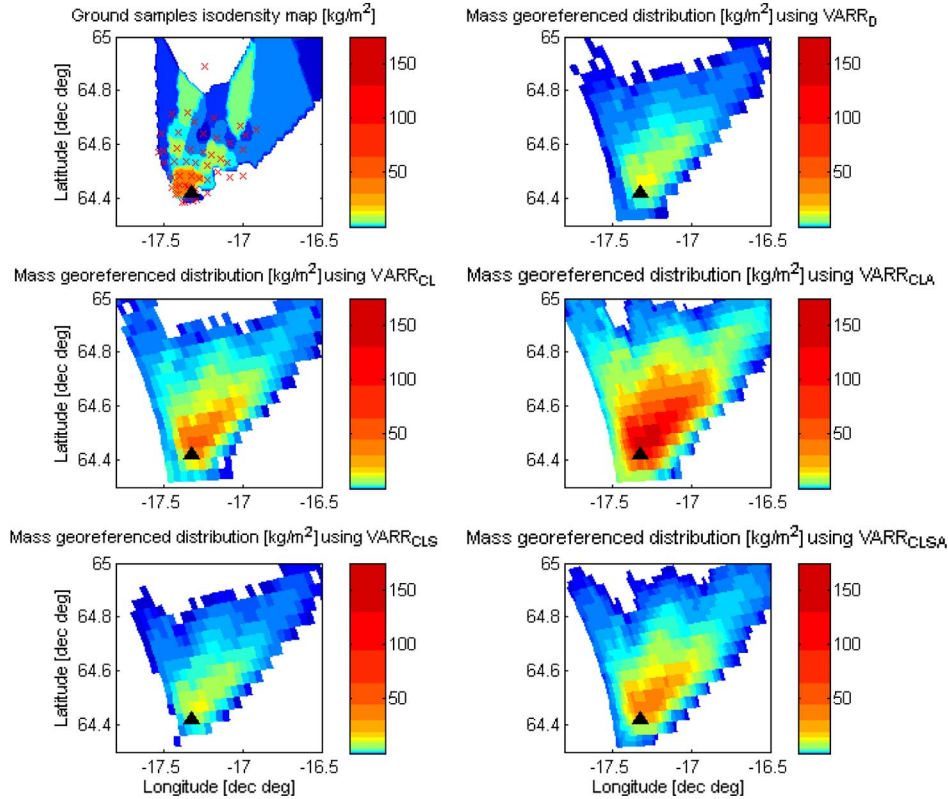


Fig. 9. Distal fallout spatial maps of the different VARR options compared to sample distribution. The left top panel shows the 69 processed sample positions; the other images show the results from the VARR versions: on the top right panel is $VARR_D$ that contains data inherited from other previously studied eruptions; on the left middle panel is $VARR_{CL}$ calibrated by using ash mean measured density, optimized PSD coefficients, and mean diameters obtained by the study of the collected sample grain size and assuming as precipitating ash fallout the last detectable value; on the right middle panel is $VARR_{CLA}$, which is a $VARR_{CL}$ version that considers also wind transport effects by means of the PCORR technique; on the left bottom panel is $VARR_{CLS}$, which is a $VARR_{CL}$ version that takes into account also the ash classes (fine ash is considered nonprecipitating); and on the right bottom panel is $VARR_{CLSA}$, which is a $VARR_{CLS}$ version that considers also wind transport effects by means of the PCORR technique. The black triangle is centered in the exact position of the Grímsvötn volcano, whereas colorbars are scaled to match the different dynamic ranges of the distributions.

resolution volumes have been reduced to 27 621 considering only ash-containing volumes (i.e., excluding all resolution volumes with ash class label value equal to 0). Coarse ash particles, as expected, are the most probable with a lower occurrence of finer particles around the volcanic caldera. On the contrary, lapilli are found in regions closer to the volcanic vent due to ballistic ejections (note that the class 9, corresponding to intense concentration of lapilli, has not been detected). Note that the low occurrence of small concentration of fine ash may be due to the weather radar observational limitations at the considered range, besides the actual ash cloud phenomena. Indeed, as well documented in [7], the radar sensitivity at C-band does not allow one to accurately quantify fine ash content at distances larger than hundreds of kilometers.

Deposited ash mass loading $D_a(x, y)$, evaluated through (18) in terms of distal spatial maps derived from radar, is shown in Fig. 9. When $VARR_{CLA}$ is compared with $VARR_{CL}$, it shows a larger area at the ground with bigger D_a values and a bigger result of the overall mass estimated value. The total mass M_{aT} from (20) and ash field spatial distribution are larger for the $VARR_{CL}$ case than for the $VARR_{CLS}$ one due to precipitating ash class selection in $VARR_{CLS}$. These VARR-estimated spatial patterns compare fairly well with ground-sampled mass loading $D_s(x, y)$ used for validation, as shown in the upper left panel in Fig. 9.

The spatial collocation of radar-based estimates and ground measurement allows pixel-by-pixel comparison between the retrieved and the deposited ash mass. This comparison should be evaluated with some care as it refers to a spatially integrated mapping from radar versus spatial interpolation of point measurements from ground sampling. Nevertheless, it is an appealing way to perform the cross-validation in terms not only of total mass but also of spatial distribution of the deposited ash. Fig. 10 shows the scatterplot of the estimated $D_a(x, y)$, obtained from $VARR_D$, $VARR_{CL}$, $VARR_{CLS}$, and $VARR_{CLA}$, as a function of the 69 corresponding ground-based mass loading values $D_s(x, y)$. As expected, the correlation is not unitary due to ground data interpolation errors and to radar-retrieval algorithm inaccuracy and obstructed geometry observation. The correlation coefficients are about 0.55, 0.55, 0.50, 0.54, and 0.49 for $VARR_D$, $VARR_{CL}$, $VARR_{CLS}$, and $VARR_{CLA}$, respectively, whereas the root mean square errors (rmse) are 27, 23, 50, 27, and 24 kg/m^2 correspondingly.

B. Ash Plume Height and EDR

The analysis of the maximum plume height H_{aM} is both an important input parameter in many volcanological models which forecast the volcanic eruption intensity and the most

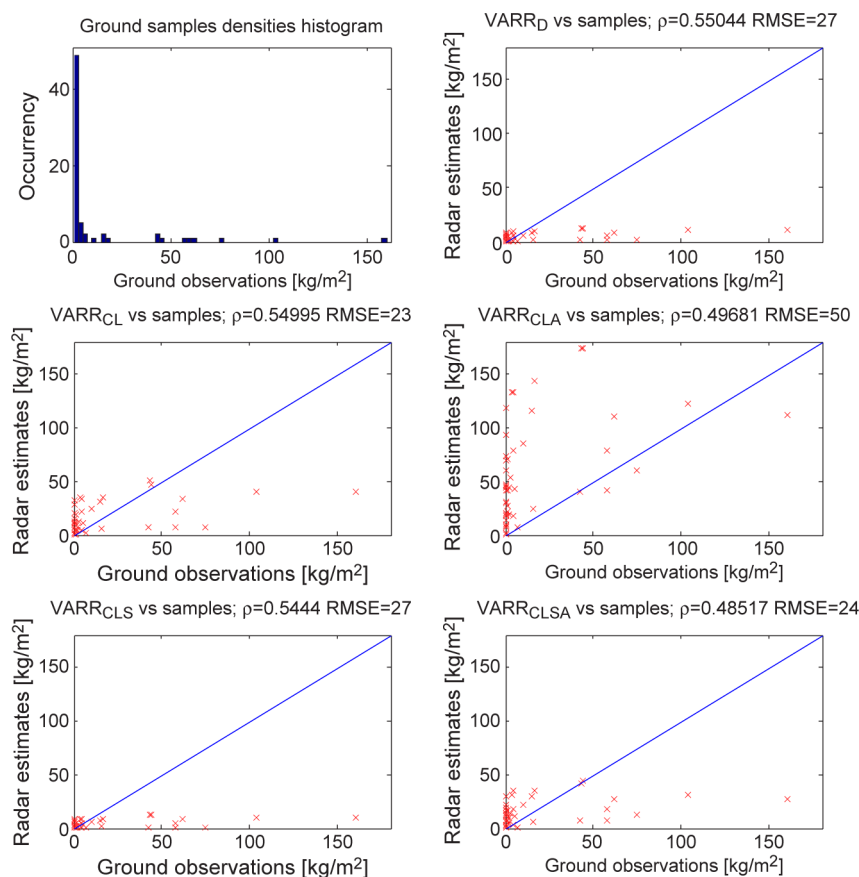


Fig. 10. Scatterplots between ground-observed and radar-estimated tephra densities for different radar-retrieval methods: VARR_D, VARR_{CL}, VARR_{CLA}, VARR_{CLS}, and VARR_{CLSA}. The upper left panel shows the distribution of tephra densities from ground observations. Correlation coefficients ρ and rmse are also quoted.

useful quantity to aerial route planning in the areas near the volcanic eruption. Plinian and sub-Plinian explosive eruptions reach their neutral level (above this height, the cloud stops its vertical growth and starts to spread radially [10]) at or above the altitude of modern commercial airplane flight level. The accurate knowledge of the maximum plume height thus lets air traffic control operators advise the pilot about the exact flight level to avoid the ash cloud. Moreover, the merging of local Volcanic Ash Advisory Center information with the information about the plume height estimated by the meteorological center is useful to produce more accurate volcanic ash significant meteorological information reports.

Using VARR in its various versions, H_{aM} (in kilometers) has been estimated, as shown in (15), by detecting the measured reflectivity Z_H or estimated concentration C_a above a threshold. The output of this retrieval step is the maximum plume height H_{aM} . The temporal evolution of the maximum plume height H_{aM} , during a time interval from 23:00 UTC on November 1, 2004, to 08:40 UTC on November 3, 2004, is shown in Fig. 11, with 5-min resolution as in Fig. 7. The three plots show the estimates of the Rainbow application software [13], installed in Keflavík radar and based on the ECHOTOP product, and the estimates of VARR_{CL} algorithm with detection thresholds on concentration ($C_a > 10^{-6}$ kg/m³) and reflectivity ($Z_{Hm} > -3$ dBZ), respectively. Rainbow data, calibrated with direct altimetric aircraft measurements, were available only within this time interval, and so, VARR_{CL} data have been cut from

440 values to 405 in order to match this time interval. Gaps in the Rainbow data have been replaced with the last detected value; the same procedure has been carried out with VARR_{CL} data in order to discard unreasonable height values (i.e., below 6 km and over 15 km). The ash estimation of VARR_{CL} shows mean values smaller than those obtained from the operational software. The latter gives results in disagreement with those of the flights during the whole eruption [13], probably because the algorithm was specifically tuned to detect water hydrometeors (which have dielectric properties different from ash particles). Note that only VARR_{CL}, using a threshold on C_a , tends to filter the anomalous peaks in the estimated maximum plume height trend. The general temporal trends of the three estimation techniques are quite similar. It is worth mentioning that historical and prehistorical ashfall records indicate that some of the largest explosive eruptions in Iceland generated ash columns up to an altitude of 20–25 km above the vent [13], [14]. These values are quite larger than those estimated by the previous considered techniques. This discrepancy may be attributed to the specific features of the 2004 eruption, but some uncertainties due to the limited radar sensitivity at far distances may play a role (particularly for the detection of the finest particles suspended at high altitudes).

The maximum plume height retrievals H_{aM} , provided by the weather radar, can be used as an input variable in models that compute the EDR, a useful parameter to mark the intensity of a volcanic eruption. The thermal energy of the erupted tephra is

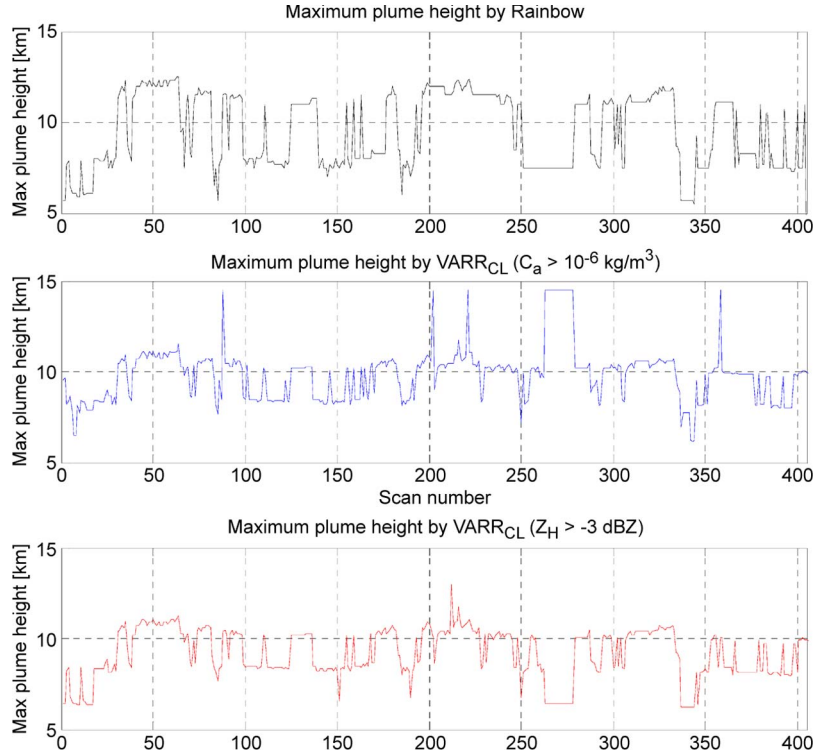


Fig. 11. Instantaneous maximum plume height versus scan number (as in Fig. 7), with input data from (upper panel) the Rainbow software and from VARR_{CL} algorithm with (middle panel) concentration and (lower panel) reflectivity thresholds. The scans start at 23:00 UTC on November 1, 2004, and end at 08:40 UTC on November 3, 2004, because the Rainbow data were available only within this time interval.

used to heat the air trapped within the eruption jet and causes convective phenomena that lead to the rise of the eruptive column. When the discharge rate is known, it is possible to estimate the thickness of the ash layer that will settle on the ground according to a model widely used for eruption columns in still air (neglecting wind effects) which produce strong plumes [10], [29], [35]. As in [34], the top height of a maintained plume from a steady source is linked to the thermal energy of the eruption by Morton's relation

$$H_{aM}(t) = 5.51 \cdot 10^{-3} (1 - n_{LC})^{-3/8} [Q_T(t)]^{1/4} \quad (25)$$

where H_{aM} (in kilometers) is the maximum plume height, Q_T (in watts) is the rate of the thermal energy production at source, and $n_{LC} = 0.663$ is defined as the ratio between the environmental lapse rate ($6.5 \text{ }^\circ\text{C/km}$) and the cooling gradient of the ash ($9.8 \text{ }^\circ\text{C/km}$), as in [29]. The thermal energy production rate Q_T is also proportional to the EDR Q_V (in cubic meters per second) through

$$Q_T(t) = \rho_m C_t (T_i - T_f) F_T Q_V(t) \quad (26)$$

where ρ_m (in kilograms per cubic meter) is the magma bulk density, C_t (in joules per kilogram kelvin) is the specific heat of the erupted tephra, T_i (in kelvin) and T_f (in kelvin) are the starting and final temperatures, and F_T is the thermal efficiency (ratio between the estimated total energy and the available thermal energy). Combining the two relations (25) and (26), it is possible to estimate the trend of the magma volume

flux Q_V versus the trend of the maximum plume height by means of

$$Q_V(t) \cong 0.085 [H_{aM}(t)]^4 \quad (27)$$

where H_{aM} is in kilometers and Q_V in cubic meters per second. The following values have been set in (26), assuming a basaltic magma: $F_T = 0.75$ from [30], $\rho_m = 2600 \text{ kg/m}^3$, $C_t = 1100 \text{ Jkg}^{-1} \text{ }^\circ\text{C}^{-1}$, $T_i = 1423 \text{ K}$, and $T_f = 273 \text{ K}$ from [31].

The relation (27) shows that the EDR is linked to the fourth power of the height, and so, small fluctuations of the height cause large variations of the discharge rate. Note that, once Q_V (in cubic meters per second) is estimated from each radar volume scan using (27), then the ash total volume V_{aQ} can be derived from

$$V_{aQ} \equiv \int_{t_i}^{t_f} V_a(t) dt \cong \Delta t_r \sum_{n=1}^{N_r} Q_V(t_n) \quad (28)$$

where N_r and Δt_r are the radar volume scan number and sampling time period. The total mass M_{aT} (in kilograms) can be evaluated through $M_{aT} = V_{aQ} \rho_{a0}$, where ρ_{a0} is the average ash density.

Discharge rate temporal trends, obtained from the operational software and VARR_{CL} with thresholds on concentration C_a and reflectivity Z_H , are shown in Fig. 12. Using the operational software, the temporal integration of the EDR gives a total mass value M_{aT} that is in agreement with the one from the estimated ground data; a similar behavior also characterizes

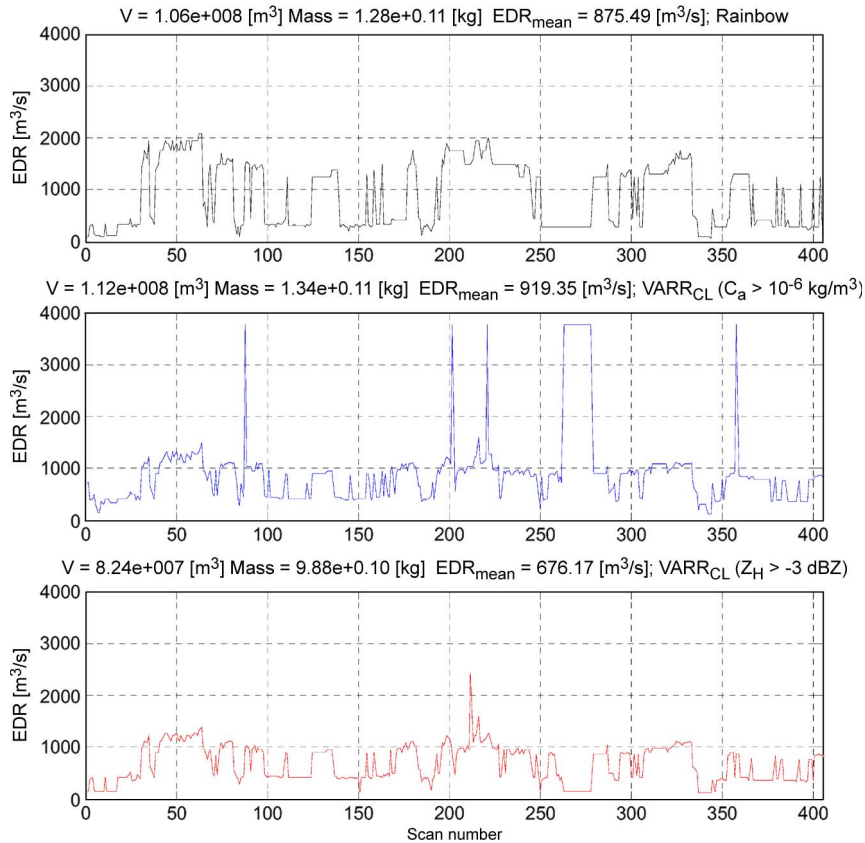


Fig. 12. Instantaneous EDR, obtained from the maximum plume height versus scan number, with input data from (upper panel) the Rainbow operational software and $VARR_{CL}$ with thresholds on (middle panel) concentration ($C_a > 10^{-6}$ kg/m³) and (lower panel) radar reflectivity factor ($Z_H > -3$ dBZ).

TABLE I

TOTAL MASS AND TOTAL VOLUME VALUES OBTAINED FROM THE FOLLOWING: 1) RADAR-DERIVED ASHFALL RATE R_a USING (18) AND (20) AND THE ALGORITHMS $VARR_D$, $VARR_{CL}$, $VARR_{CLS}$, AND $VARR_{CLA}$ AND 2) MEASURED GROUND-SAMPLED VALUES, USING (7)

Source	Total mass [kg]	Total volume [m ³]
$VARR_D$ (Default VARR)	0.36 10 ¹⁰	0.30 10 ⁷
$VARR_{CL}$ (Calibrated Lowest-bin VARR)	1.43 10 ¹⁰	1.19 10 ⁷
$VARR_{CLS}$ (Calibrated Lowest-bin Size-class VARR)	0.33 10 ¹⁰	0.27 10 ⁷
$VARR_{CLA}$ (Calibrated Lowest-bin Advection VARR)	5.72 10 ¹⁰	4.77 10 ⁷
Ground mass loading measured values	5.60 10 ¹⁰	4.70 10 ⁷

$VARR_{CL}$ estimates. It is worth stressing that $VARR_{CL}$ based on C_a threshold gives better results than the Z_{Hm} version estimate in terms of total mass when compared with the value obtained from ground sampling data.

C. Estimated Total Ash Mass and Volume

The results of $VARR_D$, $VARR_{CLS}$, and $VARR_{CL}$ with C_a and Z_H thresholds have been quantitatively compared with ground-sample data in terms of overall space–time mass M_{aT} and volume V_{aT} during the whole eruption.

From Sections II and III, the total erupted ash mass can be computed through different ways: 1) integration of the instantaneous deposited tephra $D_a(x, y)$, output of VARR and given by (18); 2) temporal integration of the discharge rate as computed by the operational software through the ash cloud maximum height, through (27); 3) temporal integration of Q_V as computed by the $VARR_{CL}$ with C_a and Z_H thresholds,

through (28); and 4) spatial integration of ground-sampled deposited tephra density, used as a validation reference and given by (6). The total volume V_{aT} or V_{sT} is then obtained from the estimated mass M_{aT} or M_{sT} , considering a mean density of the collected samples equal to 1200 kg/m³, as in (7) from ground samples and (20) from radar data. Tables I–III show the intercomparison results in terms of overall mass and volume when computed from VARR (Tables I and II) and from EDR estimates (Table III).

Table I shows, in particular, the mass and volume estimates as computed by different VARR versions ($VARR_D$, $VARR_{CL}$, $VARR_{CLS}$, and $VARR_{CLA}$) and ground measured values as reported in [17]. Table II shows the effects on total mass and volume estimation when a_v and b_v are differently chosen and whether the standard deviation of R_a is considered and then summed or subtracted to R_a . The uncertainty in the estimated R_a reflects a variability of total ash mass and volume of less than about 10% with an asymmetric behavior with respect to

TABLE II

TOTAL MASS AND TOTAL VOLUME VALUES OBTAINED FROM RADAR-DERIVED ASHFALL RATE R_a USING (18) AND (20) AND THE ALGORITHM $VARR_{CL}$ BY SELECTING FALL VELOCITY VALUES a_v AND b_v , DERIVED FROM THE EMPIRICAL MODELS IN [4] AND [36]. THE SENSITIVITY OF TOTAL MASS VOLUME TO THE STANDARD DEVIATION OF THE ESTIMATED ASHFALL RATE, INDICATED BY $\sigma(R_a)$, IS SHOWN

Source	Total mass [kg]	Total volume [m ³]
VARR_{CL} using $R_a - \sigma(R_a)$ and a_v and b_v as in	1.37 10 ¹⁰	1.14 10 ⁷
VARR_{CL} using R_a and a_v and b_v as in	1.43 10 ¹⁰	1.19 10 ⁷
VARR_{CL} using $R_a + \sigma(R_a)$ and a_v and b_v as in	1.57 10 ¹⁰	1.31 10 ⁷
VARR_{CL} using $R_a - \sigma(R_a)$ and a_v and b_v as in	1.03 10 ¹⁰	0.86 10 ⁷
VARR_{CL} using R_a and a_v and b_v as in	1.14 10 ¹⁰	0.95 10 ⁷
VARR_{CL} using $R_a + \sigma(R_a)$ and a_v and b_v as in	1.17 10 ¹⁰	0.97 10 ⁷

TABLE III

TOTAL MASS AND TOTAL VOLUME VALUES, OBTAINED BY INTEGRATING THE EDR (OR Q_V) COMPUTED FROM THE MAXIMUM PLUME HEIGHTS VIA (27) ESTIMATED BY THE FOLLOWING: 1) OPERATIONAL SOFTWARE RAINBOW; 2) $VARR_{CL}$ WITH C_a THRESHOLD; 3) $VARR_{CL}$ WITH Z_{Hm} THRESHOLD; AND 4) FROM THE MEASURED GROUND-SAMPLED VALUES

Source	Total mass [kg]	Total volume [m ³]
EDR with maximum plume height from Rainbow[®] software	12.80 10 ¹⁰	10.61 10 ⁷
EDR with maximum plume height from $VARR_{CL}$ with C_a threshold	13.41 10 ¹⁰	11.20 10 ⁷
EDR with maximum plume height from $VARR_{CL}$ with Z_{Hm} threshold	9.88 10 ¹⁰	8.24 10 ⁷
EDR with ground mass loading measured values	5.62 10 ¹⁰	4.70 10 ⁷

ash rate overestimation ($R_a + \sigma$) and underestimation ($R_a - \sigma$). The choice of a different ashfall velocity model can provide an uncertainty (underestimation) that is even larger than 30%.

Table III shows the mass and volume estimates obtained by the integration of discharge rate, derived from the maximum plume height from Rainbow, $VARR_{CL}$ (with reflectivity or concentration threshold), and ground measured values. $VARR_{CL}$ tends to provide a mass value estimation in a fairly good agreement with the measured one, whereas $VARR_D$ overestimates the total mass (not shown). With respect to the data obtained from Q_V derived from ground-sampled mass value, all algorithms slightly overestimate the total mass; indeed, $VARR_{CL}$ with C_a threshold shows a result that is fairly close to the measured one. Note that the total volume V_{aT} from Q_V estimates, using (28), can be even an order of magnitude (in cubic meters) larger than the value derived from ash density integration through (20).

V. CONCLUSION

The potential of using a ground-based C-band weather-radar system for volcanic ash cloud detection and quantitative retrieval has been quantitatively evaluated for the first time by using Vatnajökull *in situ* fieldwork data, documented in [17]. An application of the physically based VARR inversion technique has been shown, taking into consideration the eruption of the Grímsvötn volcano in Iceland in November 2004. Volume scan data from a Doppler C-band radar, located at 260 km from the volcano vent, have been processed by means of VARR. Examples of the achievable VARR products have been commented and discussed, such as the concentration or the ashfall rate. The case study has been analyzed in terms of its evolution by looking at both radar measurements and ash products, derived from the measurements themselves.

The analysis has clearly shown the unique features of radar remote sensing of volcanic eruptions. The grain size of the samples has been used to achieve a best fitting of scaled-gamma and scaled-Weibull distributions on sample measured distribution. The effects of wind transportation have been incorporated within the VARR approach using the PCORR technique, showing results of ash ground concentration, mass, and volume in accordance with *in situ* measurements. Promising results have been obtained, particularly with reference to $VARR_{CL}$ algorithm version in terms of total mass and maximum plume height estimates.

The VARR technique seems to be promising as an operational remote sensing tool for initializing physically based ash dispersion models [37] and to issue warnings on the basis of quantitative near real-time ash eruption monitoring. In an operational context, the “default” algorithm $VARR_D$ would be probably the easiest and fastest way to use radar data for retrieving ash cloud and eruption source parameters. This choice might be an acceptable compromise between accuracy of the retrieval results and data processing complexity. It should be pointed out that the effect of aggregation among ice crystals, liquid droplets, and ash particles still remains a major unknown, affecting not only microwave weather radar estimates but also ground-based lidar and satellite-based infrared techniques.

Future developments on near-vent volcanic ash retrieval should be possibly devoted to the exploitation of dual-polarized weather radar, capable of measuring polarimetric observables both in amplitude and phase. If these polarimetric radar data were available during a volcanic eruption, significant improvements of the obtained retrievals could be achieved by taking into account not only the composition of particles but also their prevailing shape and/or expected tumbling feature due to spatially random orientations during the fallout. Mixtures of hydrometeors and ash, undistinguishable from pure ash clouds

using conventional radars, could be better investigated using dual-polarization instruments [13], [20]. In this respect, weather radars at X-band might even show a better sensitivity with respect to the corresponding C-band systems having the same characteristics.

The synergy among ground- and satellite-based sensors should be further investigated as measurements from visible/infrared satellite imagers, and ground-based lidars may be used as a complementary constraint for radar-based estimates due to their high sensitivity to fine ash particles. Improvements on the ash cloud advection technique are also envisaged by computing the cross-correlation maximum within portions of all available pairs of radar maps. In this way, the estimate of a motion vector field would probably lead to a better prediction of the ash fallout spatial maps. Finally, a portable weather-radar system might overcome the limitation of observing a volcanic eruption from far distances, as in the case study here considered. The ground validation of radar-based ash estimates has been achieved by the proposed observation technique.

The VARR algorithm has turned out to be a valid approach, and with few adjustments to the monitored volcano, it may be a useful technique for airplane flight alerting in the proximity of volcanic eruptions. Proper design and deployment of an ash disdrometer network around active volcanoes, coupled with a portable microwave radar, could lead to new insights and accurate assessments of volcanic ash cloud radar remote sensing.

ACKNOWLEDGMENT

The authors would like to thank R. Hannesen (Selex SI Gematronik, Germany) and P. Crochet and S. Karlsdóttir (Iceland Meteorological Office, Iceland) for providing the radar data and Rainbow software products. The contribution of B. De Bernardinis and G. Vulpiani (DPC, Rome, Italy) and E. Picciotti (HIMET, L'Aquila, Italy) is gratefully acknowledged. The authors would also like to thank S. Pavone and S. Barbieri for contributing to the development of the VARR software and the intercomparison analysis. Most of the fieldwork was done with the support of the Iceland Glaciological Society (JÖRFÍ) during the annual spring trips in June 2005 and 2006. Important facilities were provided by the Icelandic Meteorological Office. The Grímsvötn fieldwork project was funded by The Icelandic Research Fund (Rannís), Landsvirkjun (The National Energy Company), Bílanaust, and Esso.

REFERENCES

- [1] A. J. Prata and I. J. Barton, "Hazard from volcanic ash," *Nature*, vol. 354, no. 6348, p. 25, Nov. 1991.
- [2] A. Tupper, I. Itikarai, M. S. Richards, F. Prata, S. Carn, and D. Rosenfeld, "Facing the challenges of the International Airways Volcano Watch: The 2004/05 eruptions of Manam, Papua New Guinea," *Weather and Forecasting*, vol. 22, no. 1, pp. 175–191, 2007.
- [3] A. J. Prata, "Satellite detection of hazardous volcanic clouds and the risk to global air traffic," *Nat. Hazards*, vol. 51, no. 2, pp. 303–324, 2008.
- [4] M. T. Gudmundsson, G. Larsen, Á. Höskuldsson, and Á. G. Gylfason, "Volcanic hazards in Iceland," *Jökull*, vol. 58, pp. 251–268, 2008.
- [5] D. M. Harris and W. I. Rose, Jr., "Estimating particle sizes, concentrations, and total mass of ash in volcanic clouds using weather radar," *J. Geophys. Res.*, vol. 88, no. C15, pp. 10969–10983, 1983.
- [6] C. Lacasse, S. Karlsdóttir, G. Larsen, H. Soosalu, W. I. Rose, and G. G. J. Ernst, "Weather radar observations of the Hekla 2000 eruption cloud, Iceland," *Bull. Volcanol.*, vol. 66, no. 5, pp. 457–473, 2004.
- [7] F. S. Marzano, S. Barbieri, G. Vulpiani, and W. I. Rose, "Volcanic ash cloud retrieval by ground-based microwave weather radar," *IEEE Trans. Geosci. Remote Sens.*, vol. 44, no. 11, pp. 3235–3246, Nov. 2006.
- [8] B. Oddsson, M. T. Gudmundsson, G. Larsen, and S. Karlsdóttir, "Grímsvötn 2004: Weather radar records and plume transport models applied to a phreatomagmatic basaltic eruption," in *Proc. IAVCEI*, Reykjavík, Iceland, Aug. 18–24, 2008.
- [9] G. Larsen, M. T. Gudmundsson, and H. Björnsson, "Eight centuries of periodic volcanism at the center of the Iceland hotspot revealed by glacier tephrostratigraphy," *Geology*, vol. 26, no. 10, pp. 943–946, Oct. 1998.
- [10] S. Wen and W. I. Rose, "Retrieval of sizes and total masses of particles in volcanic clouds using AVHRR bands 4 and 5," *J. Geophys. Res.*, vol. 99, no. D3, pp. 5421–5431, 1994.
- [11] H. Sauvageot, *Radar Meteorology*. Boston, MA: Artech House, 1992.
- [12] F. S. Marzano, G. Vulpiani, and W. I. Rose, "Microphysical characterization of microwave radar reflectivity due to volcanic ash clouds," *IEEE Trans. Geosci. Remote Sens.*, vol. 44, no. 2, pp. 313–327, Feb. 2006.
- [13] F. S. Marzano, S. Barbieri, E. Picciotti, and S. Karlsdóttir, "Monitoring subglacial volcanic eruption using ground-based C-band radar imagery," *IEEE Trans. Geosci. Remote Sens.*, vol. 48, no. 1, pp. 403–414, Jan. 2010.
- [14] T. Thordarson and G. Larsen, "Volcanism in Iceland in historical time: Volcano types, eruption styles and eruptive history," *J. Geodyn.*, vol. 43, no. 1, pp. 118–152, Jan. 2007.
- [15] K. Vogfjörð, S. Jakobsdóttir, G. B. Guðmundsson, M. J. Roberts, K. Ágústsson, T. Arason, H. Geirsson, S. Karlsdóttir, S. Hjaltadóttir, U. Ólafsdóttir, B. Þorbjarnadóttir, T. Skaftadóttir, E. Sturkell, E. B. Jónasdóttir, G. Hafsteinsson, H. Sveinbjörnsson, R. Stefánsson, and T. Jónsson, "Forecasting and monitoring a subglacial eruption in Iceland," *EOS*, vol. 86, no. 26, pp. 245–248, Jun. 2005.
- [16] B. Oddsson, M. T. Gudmundsson, G. Larsen, and S. Karlsdóttir, "Monitoring of the plume from the basaltic phreatomagmatic 2004 Grímsvötn eruption—Application of weather radar and comparison with plume models," *Bull. Volcanology*, Feb. 2011, submitted for publication.
- [17] B. Oddsson, "The Grímsvötn eruption in 2004: Dispersal and total mass of tephra and comparison with plume transport models," M.S. thesis, Faculty Sci., Dept. Phys., Univ. Iceland, Reykjavík, Iceland, 2007.
- [18] S. F. Stewart, H. Pinkerton, G. A. Blackburn, and M. T. Gudmundsson, "Monitoring active subglacial volcanoes: A case study using airborne remotely sensed imagery of Grímsvötn, Iceland," *Int. J. Remote Sens.*, vol. 29, no. 22, pp. 6501–6514, 2008.
- [19] M. Rennen, *Coordinate Conversion and Datum Transformation in Iceland, Manual and Technical Reference*, 2004. [Online]. Available: <http://cocodati.lmi.is/cocodati/cocodat-i.jsp>
- [20] F. S. Marzano, S. Marchiotto, C. Textor, and D. Schneider, "Model-based weather radar remote sensing of explosive volcanic ash eruption," *IEEE Trans. Geosci. Rem. Sens.*, vol. 48, no. 10, pp. 3591–3607, Oct. 2010.
- [21] C. Bonadonna, G. G. J. Ernst, and R. S. J. Sparks, "Thickness variations and volume estimates of tephra fall deposits: The importance of particle Reynolds number," *J. Volcanol. Geotherm. Res.*, vol. 81, no. 3/4, pp. 173–187, May 1998.
- [22] C. Bonadonna and B. F. Houghton, "Total grain-size distribution and volume of tephra-fall deposits," *Bull. Volcanol.*, vol. 67, no. 5, pp. 441–456, Jun. 2005.
- [23] J. Fierstein and M. Nathenson, "Another look at the calculation of fallout tephra volumes," *Bull. Volcanol.*, vol. 54, no. 2, pp. 156–167, Jan. 1992.
- [24] D. M. Pyle, "The thickness, volume and grain size of tephra fall deposits," *Bull. Volcanol.*, vol. 51, no. 1, pp. 1–15, Jan. 1989.
- [25] W. Rose, S. Bonis, R. Stobier, M. Keller, and T. Bickford, "Studies of volcanic ash from two recent Central American eruptions," *Bull. Volcanol.*, vol. 37, no. 3, pp. 338–364, Sep. 1973.
- [26] G. P. L. Walker, "The Taupo pumice—Product of the most powerful known (ultraplinian) eruption," *J. Volcanol. Geotherm. Res.*, vol. 8, no. 1, pp. 69–94, Aug. 1980.
- [27] M. Montopoli, E. Picciotti, S. Di Fabio, K. De Sanctis, G. Vulpiani, A. Gioia, P. Giordano, and F. S. Marzano, "Spectral-pyramidal advective estimation technique for radar mosaic nowcasting," in *Proc. ERAD. 6th Eur. Conf. Radar Meteorol. Hydrology*, 2010, pp. 1–6.
- [28] M. Settle, "Volcanic eruption clouds and thermal power output of explosive eruptions," *J. Volcanol. Geotherm. Res.*, vol. 3, pp. 309–324, 1978.
- [29] R. Sparks, "The dimensions and dynamics of volcanic eruption columns," *Bull. Volcanol.*, vol. 48, no. 1, pp. 3–15, Feb. 1986.
- [30] L. Wilson, R. S. J. Sparks, T. C. Huang, and N. D. Watkins, "The control of volcanic column heights by eruption energetics and dynamics," *J. Geophys. Res.*, vol. 83, no. B4, pp. 1829–1836, Apr. 1978.

- [31] R. Sparks and L. Wilson, "A model for the formation of ignimbrite by gravitational column collapse," *J. Geol. Soc. Lond.*, vol. 132, no. 4, pp. 441–451, Aug. 1976.
- [32] A. R. McBirney, *Igneous Petrology*. Burlington, MA: Jones and Bartlett Publ., 1993.
- [33] F. S. Marzano, E. Picciotti, and G. Vulpiani, "Rain field and reflectivity vertical profile reconstruction from C-band radar volumetric data," *IEEE Trans. Geosci. Remote Sens.*, vol. 42, no. 5, pp. 1033–1046, May 2004.
- [34] R. R. Morton, G. Taylor, R. R. S., and J. Turner, "Turbulent gravitational convection from maintained and instantaneous sources," *Proc. R. Soc. Lond. A, Math. Phys. Sci.*, vol. 234, no. 1196, pp. 1–23, Jan. 1956.
- [35] A. Seed, "A dynamical and spatial scaling approach to advection forecasting," *J. Appl. Meteorol.*, vol. 42, no. 3, pp. 381–388, Mar. 2003.
- [36] L. Wilson, "Explosive volcanic eruptions-II: The atmospheric trajectories of pyroclasts," *Geophys. J. R. Astron. Soc.*, vol. 30, no. 4, pp. 381–392, Dec. 1972.
- [37] C. S. Witham, M. C. Hort, R. Potts, R. Servranckx, P. Husson, and F. Bonnardot, "Comparison of VAAC atmospheric dispersion models using the 1 November 2004 Grimsvotn eruption," *Meteorol. Appl.*, vol. 14, no. 1, pp. 27–38, Mar. 2007.
- [38] U.S. Standard Atmosphere, 1976, COESA.
- [39] A. S. Jursa, Ed., *Handbook of Geophysics and the Space Environment*. Hanscom AFB, MA: Air Force Geophysics Laboratory, 1985.



Frank Silvio Marzano (S'89–M'99–SM'03) received the Laurea degree (*cum laude*) in electrical engineering and the Ph.D. degree in applied electromagnetics from the Sapienza University of Rome, Rome, Italy, in 1988 and 1993, respectively.

After being with the Italian Space Agency (ASI) and a Lecturer with the University of Perugia, Perugia, Italy, in 1997, he joined the Department of Electrical Engineering and cofounded the Centro di Eccellenza per l'Integrazione di Tecniche di Telerilevamento e Modellistica Numerica per la Previsione di Eventi Meteorologici Severi (CETEMPS), University of L'Aquila, L'Aquila, Italy. In 2005, he joined the Department of Electronic Engineering (now Department of Information Engineering, Electronics and Telecommunications), Sapienza University of Rome, where he currently teaches courses on antenna theory, electromagnetic propagation, and remote sensing. Since 2007, he has been the Vice-Director of CETEMPS, University of L'Aquila. He is a Reviewer for the major international journals in remote sensing, geoscience, and propagation. He has published more than 100 papers in international refereed journals, 30 book chapters, and more than 200 extended abstracts in conference proceedings. He coedited two books on remote sensing for *Springer-Verlag* (Berlin, Germany) in 2002 and 2010. His current research concerns passive and active remote sensing of the atmosphere from ground-based, airborne, and spaceborne platforms, development of inversion methods, radiative transfer modeling of scattering media, and radar meteorology issues. He is also involved in radio-propagation topics in relation to incoherent wave modeling, scintillation prediction, and rain fading analysis along satellite microwave links.

Dr. Marzano is a Senior Member of the IEEE Geoscience and Remote Sensing Society. Since January 2004, he has been acting as an Associate Editor of the IEEE GEOSCIENCE REMOTE SENSING LETTERS; in 2005 and 2007, he was a Guest Coeditor of the MicroRad04 and MicroRad06 Special Issues for the IEEE TRANSACTIONS ON GEOSCIENCE AND REMOTE SENSING. He was the recipient of the Young Scientist Award of the XXIV General Assembly of the Union Radio Scientifique Internationale (Osaka, Japan) in 1993, the ARPAD award from the Naval Research Laboratory (Washington, DC) in 1998, the Best Paper Award from the European Geosciences Union Plinius Conference (Nicosia, Cyprus) in 2008, and the Best Oral Paper Award on propagation from the EuCAP Conference (Berlin, Germany) in 2009. Within 2001–2005, he was the Italian national delegate for the European COST Actions n. 720 and n. 280, and since 2008, he has been the national delegate for the European COST Action projects ES702 "EGCliMet" and IC0802 "PropTNEO."



Mirko Lamantea was born in Rome, Italy, in 1986. He received the B.Sc. degree (*cum laude*) in telecommunication engineering and the M.Sc. degree (*cum laude*) in communication engineering from Sapienza University of Rome, Italy, in 2008 and 2011, respectively.

In 2010 he joined the Department of Information Engineering, Electronics and Telecommunications, Sapienza University of Rome, Italy, to cooperate on radar remote sensing of volcanic ash clouds. His current interests are passive and active environmental remote sensing, image and radar signal processing in general and electromagnetic inversion problems.



Mario Montopoli received the Laurea degree in electronic engineering from the University of L'Aquila, L'Aquila, Italy, in 2004 and the Ph.D. degree in radar meteorology from the University of Basilicata, Matera, Italy in 2008.

In 2005, he joined the Centro di Eccellenza per l'Integrazione di Tecniche di Telerilevamento e Modellistica Numerica per la Previsione di Eventi Meteorologici Severi, University of L'Aquila, as a Research Scientist on ground-based radar meteorology. Since 2006, he has been a Research Assistant with the

Department of Electrical and Information Engineering, University of L'Aquila. His main interests include precipitation retrieval, C-band radar applications and processing techniques, and spaceborne radiometry for Earth and planetary observations.

Björn Oddsson received the M.S. degree from the Institute of Earth Sciences, University of Iceland, Reykjavik, Iceland, in 2007, where he is currently working toward the Ph.D. degree, as well as carrying out the activities related to volcanic monitoring and geophysical modeling.

He is currently a Geologist and a Geophysicist with the Institute of Earth Sciences, University of Iceland.

Magnús Tumi Gudmundsson received the B.S. degree from the University of Iceland, Reykjavik, Iceland, in 1986 and the Ph.D. degree in geophysics from University College London, London, U.K., in 1992.

Between 1991 and 1995, he was with the Science Institute, University of Iceland, where he became an Associate Professor of geophysics in 1995 and a Professor in 2002. He is currently a Professor of geophysics with the Faculty of Earth Sciences, University of Iceland. Since 2008, he been acting as the Head of the Faculty of Earth Sciences and the Director of the Institute of Earth Sciences. He served as a Scientific Editor of the *Journal of Glaciology* in 2007–2010. He is the author and coauthor of about 50 reviewed papers in scientific journals and books and the coauthor of about 30 lightly or nonreviewed popular articles on scientific matters. His research interests are devoted to the following: 1) physical nature of subglacial volcanism, particularly the interaction of volcanoes and the overlying ice caps or ice sheets, including the effects on ice flow and basal water flow; 2) explosive volcanism, particularly basaltic magma–water interactions; 3) internal structure of volcanoes, particularly subglacial volcanoes and the effects of the ice volcano interaction on structure and geothermal activity; and 4) geophysical exploration, particularly gravity surveying and its application to the study of volcanic structures.

Prof. Gudmundsson has been the President of the Iceland Glaciological Society since 1998.